

Acoustic resonant oscillations between the atmosphere and the solid earth during the 1991 Mt. Pinatubo eruption

Shingo Watada¹ and Hiroo Kanamori²

Received 1 June 2010; revised 23 September 2010; accepted 5 October 2010; published 21 December 2010.

[1] Long-period harmonic Rayleigh waves were observed on seismometers during the 1991 Mt. Pinatubo eruption in the Philippines. The amplitude spectrum of the Rayleigh waves shows two distinct peaks at periods of about 230 and 270 s. In the Earth's atmosphere, long-wavelength standing acoustic waves are bounded in a low-sound-velocity channel between the thermosphere and the ground. The Rayleigh waves and the fundamental and first overtone of atmospheric acoustic waves trapped in the low-sound-velocity channels have approximately the same horizontal wavelength and frequency at periods of 230 and 270 s, respectively, i.e., the atmosphere and the solid earth satisfy the condition for acoustic resonant oscillations. The standing atmospheric long-wavelength acoustic waves set off by the eruption selectively excited seismic spheroidal modes near the resonant period through acoustic resonant coupling and resulted in harmonic Rayleigh waves. In contrast, gravity waves and Lamb waves (atmospheric boundary waves) do not couple to the ground efficiently and are not easily observed as ground disturbance on seismograms during volcanic eruptions.

Citation: Watada, S., and H. Kanamori (2010), Acoustic resonant oscillations between the atmosphere and the solid earth during the 1991 Mt. Pinatubo eruption, *J. Geophys. Res.*, 115, B12319, doi:10.1029/2010JB007747.

1. Introduction

[2] A major eruption of Mt. Pinatubo (15.14°N 120.35°E) in the Philippines occurred on 15 June 1991. *Kanamori and Mori* [1992] and *Widmer and Zürn* [1992] recognized that long-period ground motions during the eruption are dominated by oscillatory movements at distinct periods and are recorded at many worldwide seismographic networks. They confirmed from their group and phase velocities and the retrograde ground particle motion that the waves are fundamental mode Rayleigh waves radiated from Mt. Pinatubo. The observed wave trains have two distinct peaks at 230 and 270 s in the amplitude spectra. *Widmer and Zürn* [1992] also reported that similar bichromatic Rayleigh waves with periods of 195 and 266 s were radiated from the 4 April 1982 El Chichón eruption.

[3] Various mechanisms for the generation of the harmonic waves have been proposed. *Widmer and Zürn* [1992] suggested that a feedback system between local atmospheric oscillations and the eruption process are responsible for the excitation of Rayleigh waves. *Kanamori and Mori* [1992] interpreted them as the seismic Rayleigh waves excited by atmospheric oscillations set off by the eruption.

[4] If the source is the acoustic resonance of a magma chamber as suggested by *Widmer and Zürn* [1992], the

size of the chamber required to explain the observed long-period oscillations is at least several hundred kilometers and is unrealistic.

[5] *Kanamori and Mori* [1992] reported that the source phase of the observed Rayleigh waves is azimuthally independent and the oscillatory pressure change observed near Mt. Pinatubo ($\Delta = 21$ km) was about 3.5 mbar (1 bar = 10^5 Pa). They obtained the time history of the atmospheric loading near the volcano by deconvolving the observed Rayleigh waves with the synthetic ground motion computed for a delta function vertical single force. The amplitude of the atmospheric loading force is about 1.6×10^{12} N (1 N = 10^5 dyne). Assuming that the pressure change occurred simultaneously over a circular area, they roughly estimated the radius of the area to be about 40 km.

[6] *Kanamori et al.* [1994] showed that a near-source seismogram, which presumably worked as a barogram, recorded during the 1980 Mt. St. Helens eruption displayed a similar oscillation with a period of about 300 s. They tried to explain these spectral peaks observed at Mt. Pinatubo and Mt. St. Helens in terms of characteristic modes of atmospheric oscillations. They showed that in an isothermal atmosphere two distinct modes are excited by a point source in the atmosphere. They also showed that the two peaks, one at the acoustic cutoff frequency and one at a frequency less than the buoyancy frequency, appear in the amplitude spectra of near-source synthetic barograms. Based on these studies, they interpreted that the peaks of the Rayleigh wave spectra observed for the eruption of Mt. Pinatubo and of the seismogram recorded near the Mt. St. Helens eruption correspond to these two characteristic frequencies in the atmosphere.

¹Earthquake Research Institute, University of Tokyo, Tokyo, Japan.

²Seismological Laboratory, California Institute of Technology, Pasadena, California, USA.

[7] Long-period air waves in the atmosphere, with a period of about 3 ~ 30 min, from various sources such as volcanic eruptions [Pekeris, 1948; Press and Harkrider, 1966; Harkrider and Press, 1967; Mikumo and Bolt, 1985], a meteorite impact [Pekeris, 1939], ground deformation associated with a large earthquake [Mikumo, 1968; Mikumo et al., 2008] and nuclear explosions in the air have been studied by many investigators [e.g., Georges, 1968; Pierce and Posey, 1970]. These observed waves are propagating acoustic and gravity waves in the far field from the source and none of these studies addressed the energy coupling of atmospheric waves to seismic Rayleigh waves near the source. Lognonné et al. [1998] computed a long-period ground motion for a source in the air using the normal mode method. A review of long-period air waves from seismic sources is found by Mikumo and Watada [2010], and a review of atmospheric/ionospheric signals from earthquakes is given by Lognonné [2010].

[8] In this paper, we investigate (1) the acoustic coupling between seismic Rayleigh waves and atmospheric waves and (2) the excitation of Rayleigh waves by a point source in the atmosphere using the Earth's normal modes computed for a realistic spherically symmetric earth model with the solid (elastic) earth, the ocean and the atmosphere (Figure 1). The objective is to understand the excitation mechanism of the harmonic ground motions generated during the volcanic eruptions of Mt. Pinatubo and Mt. St. Helens and the energy coupling between the waves in the atmosphere and the solid earth. We will examine the simple qualitative model of Kanamori and Mori [1992] and an excitation model in an isothermal atmosphere studied by Kanamori et al. [1994]

ment (i.e., rigid) and radiation (i.e., no reflection), are considered. A volcanic eruption is simply modeled with an isotropic point source in the atmosphere. Symbols used in this paper are listed in the Notation section at the end of this paper.

2.1. Equation of Motion

[11] We ignore the effects of rotation of the Earth such as the centrifugal force and the Coriolis force because the period of waves we are interested in is much shorter than 1 day. We neglect the advection of the background medium such as wind in the atmosphere and thermal diffusion and radiation processes. We assume that fluid is inviscid. We consider that the Earth is spherically symmetric.

[12] Small oscillation problems in fluid, such as tsunami and solar oscillations are historically formulated with the Eulerian approach. Seismology treats shear and strain in elastic solid and fluid media and thus the Lagrangian approach is suitable [Aki and Richards, 1980, Box 2.3]. The normal mode problems in seismology have been treated with the Lagrangian approach. The differential equations for the eigenfunctions Z_i , $i = 1, 2, 5$, and 6, in a fluid commonly used in seismology [Saito, 1988; Woodhouse, 1988] are

$$\frac{d}{dr} \begin{pmatrix} Z_1 \\ Z_2 \\ Z_5 \\ Z_6 \end{pmatrix} = \mathbf{A} \begin{pmatrix} Z_1 \\ Z_2 \\ Z_5 \\ Z_6 \end{pmatrix}, \quad (1)$$

where A_{ij} 's are given by

$$\begin{pmatrix} -\frac{1}{r} + \frac{l(l+1)g_o}{\omega^2 r^2} & \frac{1}{\kappa} - \frac{l(l+1)}{\omega^2 \rho_o r^2} & \frac{l(l+1)}{\omega^2 r^2} & 0 \\ -\omega^2 \rho_o + \frac{l(l+1)}{\omega^2 r^2} \rho_o g_o - 4\frac{\rho_o g_o}{r} & \frac{1}{r} - \frac{l(l+1)g_o}{\omega^2 r^2} & \frac{\rho_o g_o l(l+1)}{\omega^2 r^2} - \frac{l+1}{r} & 4\pi G \rho_o \\ -4\pi G \rho_o & 0 & -\frac{l}{r} & 4\pi G \\ -\frac{(l+1)\rho_o}{r} + \frac{l(l+1)\rho_o g_o}{\omega^2 r^2} & \frac{l(l+1)}{\omega^2 r^2} & \frac{l(l+1)\rho_o}{\omega^2 r^2} & \frac{l}{r} \end{pmatrix}. \quad (2)$$

using a rigorous normal mode theory for a realistic elastic earth model surrounded by the ocean and the atmosphere.

2. Method

[9] We employ the normal mode method which has been widely used in seismology. The theories have been presented by Love [1911], Alterman et al. [1959], Takeuchi and Saito [1972], Gilbert [1980], Saito [1988], and Woodhouse [1988]. Earth models used in these studies are bounded at the surface by the ground or the ocean surface, and the atmosphere has been neglected.

[10] We extend the earth model to include the atmosphere. A top boundary is placed arbitrarily in the upper atmosphere. We include a fluid layer in the model in the same way as we do the outer core and the ocean layers. A similar approach is taken by Lognonné et al. [1998], Artru et al. [2004] and Kobayashi [2007] for the study of coupled oscillations of the atmosphere and the solid earth with a rigorous treatment of a radiation boundary condition. In the present study three types of upper boundary conditions, stress free, no displace-

$\rho_o(r)$, $g_o(r)$ and $\kappa(r)$ are reference spherical model parameters and are functions of radius, r . Quantities with a nought indicate that the quantity is perturbed during the oscillatory motion. We rederive the simultaneous differential equations (1) and (2) for the normal mode of the fluid region of the Earth in Appendix A from the Lagrangian approach. Definitions of the symbols in equation (2) are found in the Notation section. These equations are a special case of the more general six simultaneous first-order differential equations for a solid model. In a fluid Z_4 , the eigenfunction for the shear traction acting on a surface normal to the radial axis, vanishes everywhere because the shear modulus is zero. Z_3 , the eigenfunction for the horizontal displacement, is expressed explicitly as a linear combination of Z_1 , Z_2 and Z_5 , where Z_1 is the eigenfunction for the vertical displacement, Z_2 is the eigenfunction for the normal traction acting on a surface normal to the radial axis, Z_5 is the eigenfunction for the gravitational potential perturbation. By eliminating Z_3 the differential equations are reduced to equations (1) and (2) [Takeuchi and Saito, 1972; Saito, 1988]. Z_6 is the eigenfunction for the combination

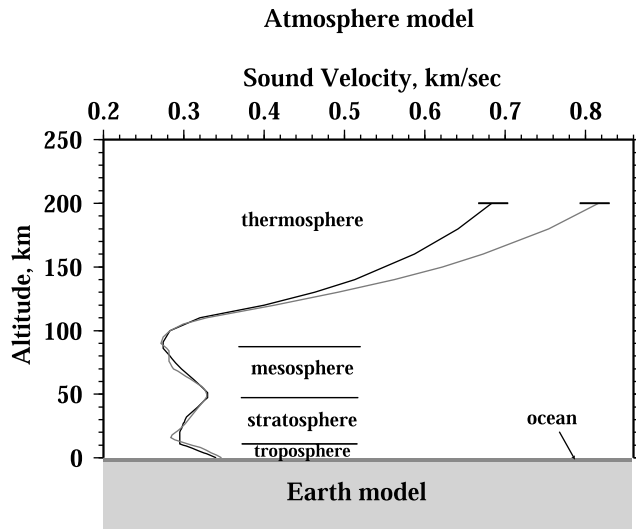


Figure 1. Atmospheric models used in this study. Black line is the *U.S. Standard Atmosphere* [1976] model. Gray line is a local atmospheric model near Pinatubo during eruption, constructed from data by *Champion et al.* [1985] (15° N July model below 90 km, 10° N June model between 90 and 110 km, 1600 K exosphere model above 110 km). Atmospheric density decreases quickly upward with a scale height of about 7 km. At 100 km, the density is about one millionth of the ground atmospheric density. The exospheric temperature of *U.S. Standard Atmosphere* [1976] approaches 1000 K. Solid earth model is PREM, not isotropic PREM, including a homogeneous ocean layer with a sound velocity of 1.45 km/s, and the uppermost crustal layer with V_p of 5.8 km/s and V_s of 3.2 km/s.

of the potential perturbation and its radial gradient and the vertical displacement, and has a convenient form to define the boundary condition for the gravity potential perturbation. See Appendix A for the exact definitions.

[13] In equation (2), note that even if model parameters ρ_o , κ , g_o , could have radial gradients the A_{ij} s do not contain the radial gradient of the earth model parameters and we can avoid numerical differentiations of the model parameters. This is the advantage of using the Lagrangian perturbation of the density and the traction. In contrast, if we took the Eulerian perturbation of the density and the traction, the

$$\frac{d}{dr} \begin{pmatrix} Z_1 \\ Z_2 \end{pmatrix} = \begin{pmatrix} -\frac{1}{r} + \frac{l(l+1)g_o}{\omega^2 r^2} & \frac{1}{\kappa} - \frac{l(l+1)}{\omega^2 \rho_o r^2} \\ -\omega^2 \rho_o + \frac{l(l+1)}{\omega^2 r^2} \rho_o g_o^2 - 4\frac{\rho_o g_o}{r} & \frac{1}{r} - \frac{l(l+1)g_o}{\omega^2 r^2} \end{pmatrix} \begin{pmatrix} Z_1 \\ Z_2 \end{pmatrix} = \mathbf{B} \begin{pmatrix} Z_1 \\ Z_2 \end{pmatrix}. \quad (3)$$

definitions of Z_2 would change and the corresponding new A_{ij} would have the radial gradients of the model parameters. The vanishing of the radial gradients of model parameters is due to the choice of the Lagrangian perturbations of density and traction and the Eulerian perturbation of gravity potential. At the first sight this seems to contradict the intuition that in a fluid the radial gradient of density should play an important role in the equation of motion as a source of

buoyancy. When a parcel in a gravitationally stratified fluid is displaced vertically, the parcel expands or contracts adiabatically according to the ambient vertical pressure profile in the fluid and changes its density. The density contrast between the displaced parcel and the surrounding fluid material is the origin of buoyancy and the expression of this term supposedly includes the vertical density gradient. However, the equations above are a set of correct equations as discussed by *Pierce* [1966] and indeed the dispersion relation of an isothermal horizontally stratified medium [e.g., *Gill*, 1982, section 6.14] can be derived, as we will see in section 2.2, from these equations by ignoring the gravity potential perturbation and using a flat Earth approximation for an isothermal atmosphere.

2.2. Local Behavior of Eigenfunctions

[14] In this section we investigate the local behavior of the eigenfunctions. For example, in 2D Cartesian coordinates (x, z) , the local behavior of sound waves expressed by $e^{i(\omega t - k_x x - k_z z)}$, is examined by the signs of k_x^2 and k_z^2 governed by the dispersion of sound waves $k_z^2 + k_x^2 = \omega^2/c^2$. For a given frequency ω , sound velocity c , and wavenumber in the x direction k_x , k_z^2 can be negative or positive. If k_z^2 is positive, the sound wave propagates in the z direction. If negative, the sound wave becomes evanescent, i.e., the wave is prohibited from propagation and the wave amplitude decays or grows in the z direction. In the high-frequency and short-wavelength limit, the effect of gravity on the equation of motion can be ignored and an eigenfunction of atmospheric waves behaves like a sound wave. At low-frequency gravity plays an important role. For atmospheric waves, the gravity perturbation caused by the density variation is very small compared to the reference gravity, elasticity and buoyancy forces.

[15] An eigenfunction in a spherical geometry with an angular order l at radius r has a real horizontal wavenumber k_h expressed by $k_h = (l + 0.5)/r$ [e.g., *Aki and Richards*, 1980, p. 356]. The radial behavior of the eigenfunction is governed by the local wavenumber in the r direction which is examined from the local dispersion relation. Note that the investigation of local behavior of the eigenfunctions is based on various approximations and is not used for the computation of eigenfunctions. Ignoring the gravity potential perturbation but including the reference gravity g_o [Cowling, 1941], the differential equations (1) and (2) become

The vertical variation of P_o and ρ_o define a local scale height H_s given by

$$\frac{1}{H_s} = -\frac{d \ln P_o}{dr} \sim -\frac{d \ln \rho_o}{dr}. \quad (4)$$

Through the middle and lower atmosphere, H_s is bounded between 6.4 km and 8.4 km at heights, z , from 0 to 86 km

and H_s is ~ 50 km at $z \sim 300$ km [Gill, 1982, section 3.5]. In order to examine the local behavior of eigenfunctions from the coefficient matrix, the rapid change of the coefficient matrix as a function of radius is not desirable. Because ρ_o and κ are the most rapidly changing variables in equation (3), and radial gradient of g_o is much smaller than those of ρ_o and κ , the vertical scale length of the B_{12} and B_{21} terms in equation (3) is about that of ρ_o or κ , or from equation (4), H_s . On the other hand the vertical scale length of the

Γ is the ratio of the specific heats, and defines the following relationships

$$\kappa = \Gamma P_o = c^2 \rho_o. \quad (15)$$

In the above, G , M , and R are constants, and M_r , U_m , c^2 and c_1 are functions of r . We rewrite equation (3) using the dimensionless quantities

$$\frac{d}{dr} \begin{pmatrix} Z_1 \\ Z_2 \end{pmatrix} = \begin{pmatrix} -\frac{1}{r} + \frac{l(l+1)}{c_1 \sigma^2 r} & \frac{4\pi R^6}{GU_m M^2 r^2} \left(c_1^2 V_g - \frac{l(l+1)c_1}{\sigma^2} \right) \\ \frac{GU_m M^2}{4\pi R^6} \left(-\frac{\sigma^2}{c_1} + \frac{l(l+1)}{\sigma^2 c_1^3} - \frac{4}{c_1^2} \right) & \frac{1}{r} - \frac{l(l+1)}{\sigma^2 c_1 r} \end{pmatrix} \begin{pmatrix} Z_1 \\ Z_2 \end{pmatrix}. \quad (16)$$

eigenfunctions can be as large as ~ 100 km, the thickness of the atmospheric layer.

[16] Here we introduce nondimensional quantities which are finite as r approaches $r = R$ where the boundary condition is imposed. Following Unno *et al.* [1989], the nondimensional quantities, U_m , V_g , c_1 , σ are

$$U_m = \frac{d \ln M_r}{d \ln r} = \frac{4\pi \rho_o r^3}{M_r} = \frac{3\rho_o}{\bar{\rho}}, \quad (5)$$

$$V_g = \frac{g_o r}{c^2} = \frac{GM_r}{c^2 r} = \frac{r}{\Gamma H_s}, \quad (6)$$

$$c_1 = \frac{r^3 M_R}{R^3 M_r} = \frac{\bar{\rho}(R)}{\bar{\rho}(r)}, \quad (7)$$

$$\sigma^2 = \frac{R^3}{GM_R} \omega^2, \quad (8)$$

where

$$M_r = \int_0^r \rho_o(r) 4\pi r^2 dr, \quad (9)$$

$$\bar{\rho}(r) = \frac{M_r}{\frac{4}{3}\pi r^3}, \quad (10)$$

$$g_o(r) = \frac{GM_r}{r^2}, \quad (11)$$

$$\frac{r}{g_o} \frac{dg_o}{dr} = \frac{4\pi \rho_o r^3}{M_r} - 2 = U_m - 2, \quad (12)$$

$$\rho_o = U_m \frac{M_r}{4\pi r^3}. \quad (13)$$

We have used Γ defined by

$$\Gamma = \frac{\rho_o}{P_o} \left(\frac{\partial P}{\partial \rho} \right)_s. \quad (14)$$

Changing the dependent variables from (Z_1, Z_2) to (X_1, X_2) which are defined by

$$X_1 = Z_1 = rU, \quad (17)$$

$$X_2 = \frac{Z_2}{\rho_o g_o} = \frac{4\pi c_1 R^6}{GU_m r M^2} Z_2, \quad (18)$$

we obtain

$$r \frac{d}{dr} \begin{pmatrix} X_1 \\ X_2 \end{pmatrix} = \begin{pmatrix} -1 + \frac{l(l+1)}{c_1 \sigma^2} & c_1 V_g - \frac{l(l+1)}{\sigma^2} \\ -\sigma^2 + \frac{l(l+1)}{\sigma^2 c_1^3} - \frac{4}{c_1} & 3 + K - U_m - \frac{l(l+1)}{\sigma^2 c_1} \end{pmatrix} \begin{pmatrix} X_1 \\ X_2 \end{pmatrix}, \quad (19)$$

$$= \mathbf{C} \begin{pmatrix} X_1 \\ X_2 \end{pmatrix}, \quad (20)$$

where

$$K = -\frac{d \ln \rho_o}{dr} r = \frac{r}{H_s}. \quad (21)$$

Now in the coefficients C_{ij} for X_1 and X_2 , rapidly changing model parameters ρ_o and κ in the r direction disappear and only c_1 , V_g , K and U_m which change slowly with r exist. Hereafter we assume that the change of C_{ij} is so small compared to the change of eigenfunctions X_1 and X_2 that C_{ij} 's are locally constant. In the atmosphere c_1 is close to 1, U_m is close to zero and V_g has a finite value of the order of 100 to 1000. Since $f(r) = r^a$ is the solution of a $rd f(r)/dr = af(r)$ type differential equation, we assume that X_1 and X_2 locally depend on r in polynomial form as r^λ . Replacing c_1 by 1 and U_m by 0, the characteristic equation for equation (20)

$$\lambda^2 - (C_{11} + C_{22})\lambda + C_{11}C_{22} - C_{12}C_{21} = 0 \quad (22)$$

is simplified to

$$\lambda^2 - (2 + K)\lambda - \left(\frac{l(l+1)}{\sigma^2} - V_g \right) (\sigma^2 - K + V_g) - \left(V_g^2 - V_g(K + 4) + 3 + K \right) = 0 \quad (23)$$

and its solutions are

$$\lambda_{\pm} = \frac{1}{2}(2 + K \pm \sqrt{\gamma}), \quad (24)$$

where

$$\gamma = (K - 2V_g + 4)^2 + 4\left(\frac{l(l+1)}{\sigma^2} - V_g\right)(\sigma^2 - K + V_g). \quad (25)$$

Using the normalized buoyancy frequency A^*

$$A^* = \frac{N^2 r}{g_o} = -\left(\frac{r}{\rho_o} \frac{d\rho_o}{dr} + \frac{g_o r}{c^2}\right), \quad (26)$$

$$= K - V_g, \quad (27)$$

where N is the buoyancy frequency (or Brunt Väisälä frequency), equation (25) is expressed as

$$\gamma = (A^* - V_g + 4)^2 + 4\left(\frac{l(l+1)}{\sigma^2} - V_g\right)(\sigma^2 - A^*). \quad (28)$$

Unno *et al.* [1989] who used the Eulerian pressure perturbation as a dependent variable instead of the Lagrangian pressure perturbation reached the same characteristic equation. In this characteristic equation the radial gradient of model parameters is indeed included through $K = r/H_s$. The energy density of a mode, $E = \rho_o \left(\frac{du}{dt}\right) \cdot \left(\frac{du}{dt}\right)^\dagger = \rho_o |\omega|^2 |\mathbf{u}|^2$, where \dagger denotes the complex conjugate, is given by

$$E = \rho_o |\omega|^2 \left(|U|^2 + l(l+1) |V|^2 \right) Y_l^m(\theta, \varphi)^\dagger Y_l^m(\theta, \varphi), \quad (29)$$

$$\propto \rho_o |\omega|^2 \left(\frac{|X_1|^2}{r^2} + \frac{l(l+1)}{r^2 \sigma^4} (|X_1 - X_2|^2) \right), \quad (30)$$

$$\propto r^{-K-2} r^{2\lambda_{\pm}} = r^{\pm\sqrt{\gamma}}, \quad (31)$$

$$\propto e^{\pm \frac{r-r_o}{r_o} \sqrt{\gamma}}. \quad (32)$$

From equation (31) to equation (32) we have approximated an exponential function of r , $\exp(-ar)$, by a power function of r , $(re/r_o)^{-ar}$. Two functions have the same value and gradient at $r = r_o$, where a is a constant and r_o is the radius where the eigenfunction is locally examined. If $\gamma > 0$, two evanescent solutions of the growing and decreasing modal energy with altitude exist. At the top boundary the solution of the growing modal energy associated with λ_+ is rejected and the modal energy decreases exponentially with altitude near the top because we assume the source of the modal energy is below the top boundary. If $\gamma < 0$, the two propagating wave-type solutions associated with λ_+ and λ_- represent waves whose vertical phase velocities are downward and upward, respectively, because we assumed that eigenfunctions have time dependence $e^{i\omega t}$. For a given atmospheric model, γ is a function of local model para-

meters and the period and the horizontal wavelength of the mode, and can be written as

$$\gamma(r, \omega, k_h) = -\frac{4V_g}{\sigma^2} \left(\left(\sigma^2 - \frac{l(l+1)}{V_g} \right) (\sigma^2 - K + V_g) - (K - 2V_g + 4) \frac{\sigma^2}{4V_g} \right), \quad (33)$$

$$= -\frac{4V_g}{\sigma^2} (\sigma^2 - \sigma_1^2) (\sigma^2 - \sigma_2^2). \quad (34)$$

$\sigma_1(r, k_h)$ and $\sigma_2(r, k_h)$ are the roots of the right-hand side of equation (33). Because $\frac{l(l+1)}{V_g} > 0$, $\frac{(K-2V_g+4)^2}{4V_g} > 0$ and for a stably stratified fluid

$$K - V_g = A^* = \frac{N^2 r}{g_o} > 0 \quad (35)$$

holds, the two positive real frequencies σ_1 and σ_2 ($\sigma_1 < \sigma_2$) always exist for any subadiabatic atmospheric model. As we see below, $\sigma_1(r, k_h)$ corresponds to the buoyancy frequency as $k_h \rightarrow \infty$, and $\sigma_2(r, k_h)$ corresponds to the acoustic cutoff frequency as $k_h \rightarrow 0$. Waves are evanescent for $\sigma_2 > \sigma > \sigma_1$ and are propagating vertically for $\sigma_2 < \sigma$ or $\sigma_1 > \sigma$, therefore σ_1 and σ_2 are called the cutoff frequencies. We have the following asymptotic values of the regime boundaries ($\gamma = 0$) between the propagating regime and the evanescent regime in the frequency-horizontal wavenumber domain:

$$\text{when } l \rightarrow 0, \sigma_1^2 \rightarrow 0 \text{ and } \sigma_2^2 \rightarrow A^* + \frac{(A^* - V_g + 4)^2}{4V_g}, \quad (36)$$

$$\text{when } l \rightarrow \infty, \sigma_1^2 \rightarrow A^* \text{ and } \sigma_2^2 \rightarrow \frac{l(l+1)}{V_g}, \quad (37)$$

or equivalently

$$\text{when } l \rightarrow 0, \omega_1^2 \rightarrow 0 \text{ and } \omega_2^2 \rightarrow N^2 + c^2 \left(\frac{1}{2H_s} - \frac{g_o}{c^2} + \frac{2}{R} \right)^2, \quad (38)$$

$$\text{when } l \rightarrow \infty, \omega_1^2 \rightarrow N^2 \text{ and } \omega_2^2 \rightarrow \frac{l(l+1)c^2}{R^2}. \quad (39)$$

These local cutoff frequencies are indeed the same as those of an isothermal atmosphere [e.g., Gill, 1982, Figure 6.18] if $R \gg H_s$,

$$\text{when } k_h \rightarrow 0, \omega_1^2 \rightarrow 0 \text{ and } \omega_2^2 \rightarrow N^2 + c^2 \left(\frac{1}{2H_s} - \frac{g_o}{c^2} \right)^2 = \left(\frac{c}{2H_s} \right)^2 = N_A^2, \quad (40)$$

where N_A is the acoustic cutoff frequency and k_h is the horizontal wavenumber.

[17] The rate of vertical flow of energy per unit area, F_r , is given by, e.g., Gill [1982, equation (4.6.4) neglecting viscosity] the radial component of the real part of

$$\mathbf{F} = \left(p' + \frac{1}{2} |\mathbf{v}|^2 \right) \mathbf{v}^\dagger, \quad (41)$$

where $\mathbf{v} = \frac{d\mathbf{u}}{dt}$, Lagrangian velocity of the material element. For a small oscillation, F_r is approximated [Watada, 2009] by $F_r = p'(\frac{du_r}{dt})^\dagger$

$$\text{Re}(F_r) = \text{Re}\left(-i\omega p' u_r^\dagger\right), \quad (42)$$

$$\propto \text{Re}\left[-i\omega \frac{\rho_0 g_0}{r^2} (X_1 X_1^\dagger - X_2 X_1^\dagger)\right]. \quad (43)$$

Eliminating X_2 by equation (20) and using polynomial expression of X_1 we have

$$\left(V_g - \frac{l(l+1)}{\sigma^2}\right) \text{Re}(F_r) \propto \text{Re}\left[-i\omega \frac{\rho_0 g_0}{r^2} (V_g - 1 - \lambda_\pm) |X_1|^2\right], \quad (44)$$

$$\propto -\text{Im}(\lambda_\pm), \quad (45)$$

$$\propto -\text{Im}(\pm\sqrt{\gamma}), \quad (46)$$

where the upper and lower signs correspond to the downward (λ_+) solution and upward (λ_-) solution, respectively. Interpreting equation (46), we have the following results. Vertical energy flow does not exist when $\gamma \geq 0$, i.e., where waves are locally evanescent. The sign of vertical energy flow depends on the sign of $\text{Im}(\sqrt{\gamma})$ and the sign of $(V_g - l(l+1)/\sigma^2)$. When $V_g > l(l+1)/\sigma^2$ or equivalently $\omega^2 > L_l^2$, vertical wave energy flow, upward or downward, requires vertical phase propagation, upward (λ_-) or downward (λ_+), respectively. Here we have introduced the Lamb frequency L_l defined by

$$L_l^2 = \frac{l(l+1)}{r^2} c^2. \quad (47)$$

For large l , $\omega^2 > L_l^2$ corresponds to propagating acoustic waves. Since we reject the solution with downward energy flow, an appropriate solution always has an upward vertical phase velocity (λ_- solution). When $V_g < l(l+1)/\sigma^2$ or equivalently $\omega^2 < L_l^2$, wave energy flow upward or downward requires phase propagation downward or upward, respectively. Similarly rejecting the downward energy flow, an appropriate solution always has a downward vertical phase velocity (λ_+ solution). The opposing direction between the vertical phase velocity and the vertical energy flow is characteristic of propagating gravity waves in both compressible and incompressible fluid [e.g., Gill, 1982, section 6.14; Watada, 2009].

[18] There is a modal branch corresponding to surface gravity waves indicated by tsunami in Figure 6 for an earth model with the ocean layer at the top. This tsunami branch crosses the propagating gravity wave regime and the evanescent regime of the atmospheric waves in the frequency horizontal wavenumber domain (Figure 2c). The coupling between tsunami in the ocean and the propagating gravity waves in the atmosphere is discussed in section 7.

[19] In summary, acoustic modes ($\omega > \omega_2$), which approach sound waves in the short horizontal wavelength limit, have an upward vertical phase velocity and upward energy transport. Evanescent modes ($\omega_2 > \omega > \omega_1$) have zero upward vertical phase velocity and no vertical energy

transport. Gravity modes ($\omega_1 > \omega$), whose eigenperiod approaches the buoyancy frequency in the short-wavelength limit, have a downward vertical phase velocity and upward energy transport. The locally defined quantity γ in equations (25), (28) and (33) diagnoses the local behavior of waves in the vertical direction for a given period and horizontal wavelength. In the region where γ is negative, waves are trapped or propagating depending on the boundary condition. In the region where γ is positive, waves become evanescent and the modal energy density decays or increases exponentially in the vertical direction. Analyses in this section are valid when the vertical scale length of waves is shorter than that of γ . As the vertical scale length of γ approaches the vertical wavelength of atmospheric waves, the analyses become less accurate.

2.3. Computation of Normal Mode

2.3.1. Conventional Upper Boundary Conditions

[20] Under the Cowling approximation [Cowling, 1941], the free upper boundary condition is satisfied by setting Z_2 to zero, and the nonvertical displacement boundary or rigid boundary condition is satisfied by setting Z_1 to zero. When the gravitational potential perturbation is included, an additional boundary condition $Z_6 = 0$ must be imposed. The determinant of the two sets of dependent solutions at the boundary is computed. The boundary condition is satisfied when the determinant vanishes [Takeuchi and Saito, 1972].

2.3.2. Radiation Upper Boundary Condition

[21] The radiation boundary condition imposes a relation between the eigenfunctions. Once λ is evaluated at the radiation boundary by equation (24), from equations (17), (18) and (20) for an evanescent mode with $\omega_2 > \omega > \omega_1$,

$$(C_{11} - \lambda_-)Z_1 + C_{12} \frac{Z_2}{\rho_0 g_0} = 0 \quad (48)$$

or

$$C_{21}Z_1 + (C_{22} - \lambda_-) \frac{Z_2}{\rho_0 g_0} = 0 \quad (49)$$

is the boundary condition. The eigenfrequencies and eigenfunctions are real. For an acoustic mode with $\omega > \omega_2$ or a gravity mode with $\omega < \omega_1$,

$$(C_{11} - \lambda)Z_1 + C_{12} \frac{Z_2}{\rho_0 g_0} = 0 \quad (50)$$

or

$$C_{21}Z_1 + (C_{22} - \lambda) \frac{Z_2}{\rho_0 g_0} = 0 \quad (51)$$

is the boundary condition. The eigenfrequencies and the eigenfunctions become complex. We choose $\lambda = \lambda_+$ or λ_- to satisfy the radiation boundary condition that inhibits downward energy flow through the upper boundary. If we define $\sqrt{\gamma}$ with $\text{Im}(\sqrt{\gamma}) \geq 0$, from the discussion in section 2.2, λ_- is the appropriate boundary condition for acoustic modes, and λ_+ is the appropriate boundary condition for gravity modes. The boundary condition for the propagating modes is treated a little differently by Unno *et al.* [1989]. They set the boundary condition where modal energy density E in

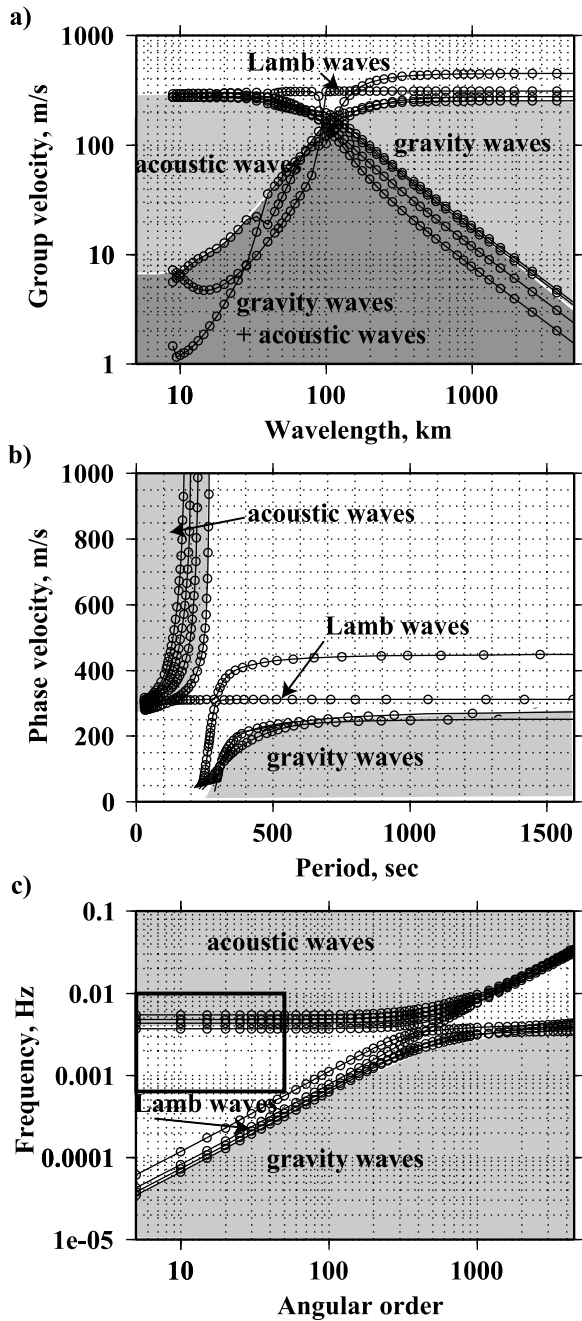


Figure 2. Normal modes of the *U.S. Standard Atmosphere* [1976] model in Figure 1. The top boundary at 200 km is a stress-free surface boundary and the bottom is a rigid boundary. Three major groups of eigenmodes exist. Acoustic modes are the sound waves in the atmosphere. Gravity modes exist for a fluid body under gravity with subadiabatic density stratification, such as the Earth’s atmosphere. Lamb waves are boundary waves which travel along the ground with the speed of sound. (a) Horizontal wavelength versus horizontal group velocity. Acoustic and gravity wave regimes overlap. (b) Period versus horizontal phase velocity for comparison with early studies. The horizontal phase velocity is computed by $\omega r_e / (l + 0.5)$, where $r_e = 6371$ km. (c) Angular order versus frequency. The boxed region is magnified in Figure 7.

equation (32) does not grow or decay locally by adjusting the value of λ_{\pm} . Their set of complex eigenfrequency σ , complex γ and complex λ do not satisfy the characteristic equation (equations (22), (23), (24) and (25)).

2.3.3. Lower Boundary Conditions

[22] To compute atmospheric modes neglecting the ocean and the solid earth, the bottom boundary of the atmosphere is assumed rigid by setting Z_1 to 0. For modes whose eigenfunctions start beneath the ocean or ground surface, such as seismic Rayleigh waves and the modes for an earth model including the atmosphere, the boundary values of eigenfunctions at a starting level are obtained from the analytic solution of an isotropic homogeneous fluid or solid body whose model parameters are the same as those at the boundary [Pekeris and Jarosch, 1958; Takeuchi and Saito, 1972]. The appropriate starting level of the integration is where the amplitudes of the eigenfunctions become so small that the ratio of amplitude at the starting level relative to the maximum amplitude reaches a preset computational accuracy. Such a starting level is roughly estimated by integrating the radial wavenumber of a mode from the starting level to the turning level of the corresponding seismic ray. For example, an acoustic/seismic spherical wave with angular order l has a vertical wavenumber k_r at r which is given by $k_r^2 = \omega^2/c(r)^2 - l(l + 1)/r^2$. Above, at, or below the turning point of the acoustic/seismic ray corresponding to this spherical wave, k_r^2 is real, zero, or imaginary, respectively. Below the turning point, the wave amplitude decay is roughly estimated by $\exp(-\int_{r_s}^{r_t} \sqrt{-k_r^2} dr)$, where r_s and r_t are the integration starting and ray turning radii, respectively.

2.3.4. Integration

[23] We use a shooting method to compute the normal modes. The differential equations for a fluid body (equations (1) and (2)) are integrated from a starting level to a boundary level. The compound matrix method [Takeuchi and Saito, 1972], or equivalently the minors method [Woodhouse, 1988], is not used. In a solid, the equations of motion are expressed to six (or four if the Cowling approximation is used) simultaneous first-order differential equations. The connection of eigenfunctions at the solid–fluid boundary is described by Takeuchi and Saito [1972]. The connection of eigenfunctions at the fluid–fluid boundary at the surface of the ocean is similarly derived. For the radiation upper boundary condition complex eigenfrequencies and eigenfunctions are obtained by a complex root search [Friedman, 1966]. We employ an adaptive step size control Runge-Kutta integrator [Press et al., 1992]. Model parameters are given as a table at discrete points. Between the grid points the model parameters are linearly interpolated. Since the program controls the integration step size, a uniform accuracy of the eigenfunctions can be maintained easily. For an eigenfunction with the free surface boundary or rigid boundary condition, the numerical integration accuracy is crudely tested by the energy integrals [Takeuchi and Saito, 1972].

[24] When the integration is performed in a relatively thick region where γ has large positive values and the modal energy is decreasing in the direction of integration, the integration becomes numerically unstable because the unwanted solution grows exponentially [Press et al., 1992]. However, the eigenvalue is accurately computed for this distorted eigenfunction because this growing component is the other solution with the same eigenvalue [Jensen et al., 1994]. For

gravity modes with large angular order numbers, the modal energy is trapped sometimes locally, e.g., near the mesopause, and the one-way integration becomes unstable. For these cases we integrate from the bottom boundary upward and from the top boundary downward and match the two sets of eigenfunctions at a level where the modal energy is trapped. For low-order acoustic modes we can stably integrate both upward and downward by the adaptive step size Runge-Kutta integration because $|\gamma|$ is relatively small. The horizontal group velocity is obtained by numerical differentiation along the modal branch or, if the boundary condition is free or rigid, by integral relations [Takeuchi and Saito, 1972].

3. Normal Modes in the Atmosphere

[25] Figure 1 shows the acoustic velocity profile of the atmosphere models used in this study. The sound velocity is computed from the temperature and the pressure by $c^2 = \Gamma P_o / \rho_o$. We assume that Γ is constant, 1.4, the value for ideal diatomic molecule gas [e.g., Gill, 1982]. We cross-checked the eigenfrequencies of atmospheric modes computed by the Runge-Kutta method in section 2.3.4 with those computed using the Haskell matrix method [Press and Harkrider, 1962], and group velocities computed by the method in section 2.3.4 with those computed using the partial derivatives of the Haskell matrix [Harkrider, 1964]. The Haskell matrix method is applied for an atmosphere model composed of stacked isothermal layers. Figure 2 shows the normal modes for the *U.S. Standard Atmosphere* [1976] model. The cutoff frequencies computed at $z = 100$ km and 200 km are plotted in Figure 3. In the nonrotating spherically symmetric atmosphere, three types of waves exist, acoustic waves, Lamb waves and internal gravity waves. Many references on atmospheric acoustic waves, the Lamb waves and internal gravity waves can be found in, for example, Lamb [1910], Beer [1974] and Georges [1968]. The horizontal group velocity of a mode can be roughly obtained from the slope of the branch in the (frequency-angular order number) plot (Figure 2c). All the computed normal modes for the atmosphere fall into these three categories except surface gravity waves along a deep-water-wave-like branch in the atmosphere which is an artifact of the top free surface boundary. These artificial modes are excluded from Figure 2.

[26] In the frequency band in which the harmonic seismic surface waves were observed during the eruption of Mt. Pinatubo, about 200 ~ 300 s, all three types of atmospheric waves can exist. They are long-wavelength acoustic waves near the acoustic cutoff frequency, Lamb waves and short-wavelength gravity waves near the buoyancy frequency, or the Brunt-Väisälä frequency. Kanamori et al. [1994] suggested that the acoustic modes near the acoustic cutoff frequency and the gravity modes near the buoyancy frequency can be excited efficiently by a volcanic eruption. The efficiency of the coupling between the atmospheric waves excited by a volcanic eruption and the seismic waves (and tsunami if including the ocean) in the solid earth are controlled by the wave period and the wavelength along the interface. Efficient coupling is expected between two waves above and below the interface when they have a common phase velocity along the interface. Group velocity alone cannot be used as an indicator of the coupling efficiency between two waves. For the long-wavelength acoustic modes

near the acoustic cutoff, the longer the wavelength, the larger the horizontal phase velocity and the smaller the horizontal group velocity. For example in Figure 2, at angular order 30 or horizontal wavelength 1300 km, the gravest three acoustic modes have a horizontal phase velocity of about 4 ~ 5 km/s and a horizontal group velocity of about 10 m/s. Short-wavelength gravity modes, for example at $l = 2000$ (wavelength = 20 km), near the cutoff have small horizontal phase velocity ≤ 100 m/s and horizontal group velocity ≤ 10 m/s.

[27] The waveforms in the far-field barographic records [e.g., Press and Harkrider, 1962; Harkrider, 1964; Mikumo, 1968; Mikumo and Bolt, 1985; Mikumo et al., 2008] were dominated by the Lamb waves, which propagate at the speed of sound. A few branches of acoustic and gravity modes, whose group and phase velocities are close to the sound velocity in the atmosphere, are required in the computation to simulate the barographic observations [Harkrider, 1964]. In this paper, we call all atmospheric modes whose modal energy is concentrated toward the surface of the ground, or the ocean, Lamb wave modes. The Lamb mode branch crosses the acoustic and gravity branches (Figure 2a).

[28] Kanamori and Mori [1992] and Kanamori et al. [1994] reported harmonic barographic pressure changes recorded during the eruptions of Krakatoa 1883, Mt. St. Helens 1980 and Mt. Pinatubo 1991. Table 1 summarizes harmonic oscillations found in barograms and seismograms during these major volcanic eruptions.

[29] The modal energy density of long-wavelength ($l = 30$, wavelength = 1300 km) acoustic modes near the cutoff frequency is shown in Figure 4. The gravest mode with a period of 329 s has its energy only in the thermosphere. For this period and horizontal wavelength, a standing or propagating wave may exist in the thermosphere and the troposphere where γ is negative. To have a standing wave in a negative γ 'well', we require from equation (32)

$$h \frac{\sqrt{-\bar{\gamma}}}{r_o} = n\pi, \quad (52)$$

where $\bar{\gamma}$ is the average of γ in the negative γ region, h is the vertical extent of the negative region and n is a positive integer. The negative γ region in the troposphere does not hold a standing wave because the vertical scale of the troposphere is too small to have a standing wave in this region and only a propagating wave exists in the thermosphere for this model. When we take the top boundary at $z = 100$ km, this mode disappears.

[30] The second gravest mode with a period of 274 s, which is close to one of the observed periods (Table 1), is a trapped mode. The positive γ region in the mesopause, the low-velocity channel which forms the boundary layer between the thermosphere and mesosphere, works as a wave-reflecting wall for this mode and the modal energy is trapped below the mesopause and above the ground (Figure 1).

[31] The third gravest mode with a period of 236 s, which is also close to one of the observations, has a large energy concentration below the thermosphere where γ has larger negative values than in the upper atmosphere. Because γ is negative everywhere, the modal energy can leak into the upper atmosphere. For this type of mode a radiation boundary condition is necessary.

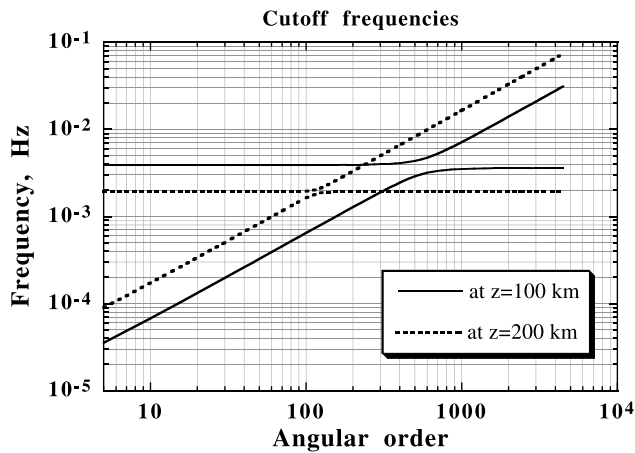


Figure 3. Cutoff frequencies ω_1 and ω_2 ($\omega_1 < \omega_2$) for the U.S. Standard Atmosphere [1976] model computed at $z = 100$ km and 200 km. In the region where $\omega_2 > \omega > \omega_1$, waves become evanescent. In the region where $\omega > \omega_2$ or $\omega < \omega_1$, propagating acoustic or gravity waves exist, respectively. The cutoff frequencies change mainly because atmospheric temperature changes with altitude. As altitude changes, the wave characteristics of (l, ω) could change from a propagating wave to an evanescent wave and vice versa.

[32] The energy distribution of higher-frequency acoustic modes changes with altitude like a \cos^2 standing wave type oscillation. This standing wave type oscillation is an artifact caused by the reflection at the top free surface boundary; if we remove the reflecting boundary at the top, then the modal energy will smoothly propagate upward or downward through the boundary. The oscillation of trapped modes represents the reverberation of sound waves in the negative γ well and may be a source of the temporal harmonic loading on the ground. At higher frequencies, because upward short-period acoustic waves do not come down by reflection, acoustic reverberation in the atmosphere may not exist and cannot be a source of harmonic loading. The harmonic ground motions with periods of 270 s and 230 s recorded on seismograms throughout the world are most likely the trapped acoustic modes that coupled to the ground.

[33] The short-wavelength gravitational modes ($l = 2000$, wavelength = 20 km) (Figure 4) have concentrated modal energy at higher altitude near $z = 100$ km except one mode. The mode with a period of 300 s has energy concentration in the stratosphere. A low-altitude source such as a volcanic eruption may preferentially excite this mode and the periodic pressure change with a period of 300 s may be recorded at the ground level. Because of its small horizontal group velocity, the pressure change associated with this gravity mode will be observed near the volcano. The atmospheric oscillation with a period near 300 s observed by a seismometer which worked as a barograph near Mt. St. Helens just after the explosive eruption in 1980 may be this type of gravity mode trapped in the stratosphere. A satellite infrared image of Mt. Pinatubo during the 1991 eruption shows [Kanamori *et al.*, 1994, Figure 11] a concentric pattern of temperature disturbance with wavelength of several tens of kilometers around the volcano extending over a distance

of about 400 km. If we assume that the waves in the satellite image have the period of about 300 s, the concentric pattern probably represents the gravity waves excited by the volcanic eruption, because acoustic waves and Lamb waves should have much shorter periods at the wavelength of several tens kilometers (Figure 2).

[34] The choice of the top boundary type and its location are not important if a mode is naturally trapped, or ducted, below the top boundary by ‘wall’ layers which have positive γ . Our numerical computation confirms that the 270 s acoustic mode always exists for any type of top boundary if placed at higher than 100 km (Figure 5). The mode always hits a natural boundary near $z = 100$ km and its modal energy is confined between $z = 0$ and about 100 km.

[35] The local atmospheric structure can deviate from the standard atmosphere model diurnally, seasonally, geographically and latitudinally [Champion *et al.*, 1985]. In the thermosphere the temperature is mainly controlled by the solar activity [COSPAR Working Group IV, 1972]. These variations may result in the change of not only eigenperiod but also the energy density distribution of modes; as a result a trapped mode may become a propagating mode and vice versa. In Table 2 we list the result of computation for an atmospheric structure close to the local model during the eruption of Mt. Pinatubo in 1991 plotted in Figure 1.

[36] The local atmospheric model near Mt. Pinatubo in June has two distinct features. Low temperature, about 10 K lower than the average at the bottom of the stratosphere, and high thermospheric temperature, about 500 K higher. We choose the high thermospheric temperature because the solar activity was high in 1991. The eigenperiods of the four trapped acoustic modes change slightly. Two gravity modes with energy trapped in the stratosphere exist with distinct eigenfrequencies. A higher temperature in the thermosphere results in the increase of γ , but still negative, and the modal energy density decreases more near $z = 200$ km than those for the standard atmosphere, and the second overtone of the acoustic mode becomes nearly trapped. We speculate that the observed period 195 s during the 1982 El Chichón eruption may be a trapped acoustic mode when the solar activity was extremely high. In fact, in 1982 its cycle was near the peak. However, the reason why the amplitude spectrum peak near 230 s is missing in the seismographic observation during the 1982 El Chichón eruption remains unexplained.

4. Normal Modes in the Earth

[37] We use the Preliminary Reference Earth Model (PREM) of Dziewonski and Anderson [1981] for the solid earth. The normal modes of PREM are shown in Figure 6.

Table 1. Observations of Harmonic Atmospheric Oscillations and Harmonic Ground Motion During Major Volcanic Eruptions^a

Eruption	Period	Observation Method	Distance
1991 Pinatubo	270 s, 230 s	seismograph	teleseism
1982 El Chichón	195 s, 266 s	seismograph	teleseism
1980 Mt. St. Helens	~300 s	seismograph worked as barograph	near source
1883 Krakatoa	~300 s	barograph	near source

^aCompiled by Kanamori *et al.* [1994].

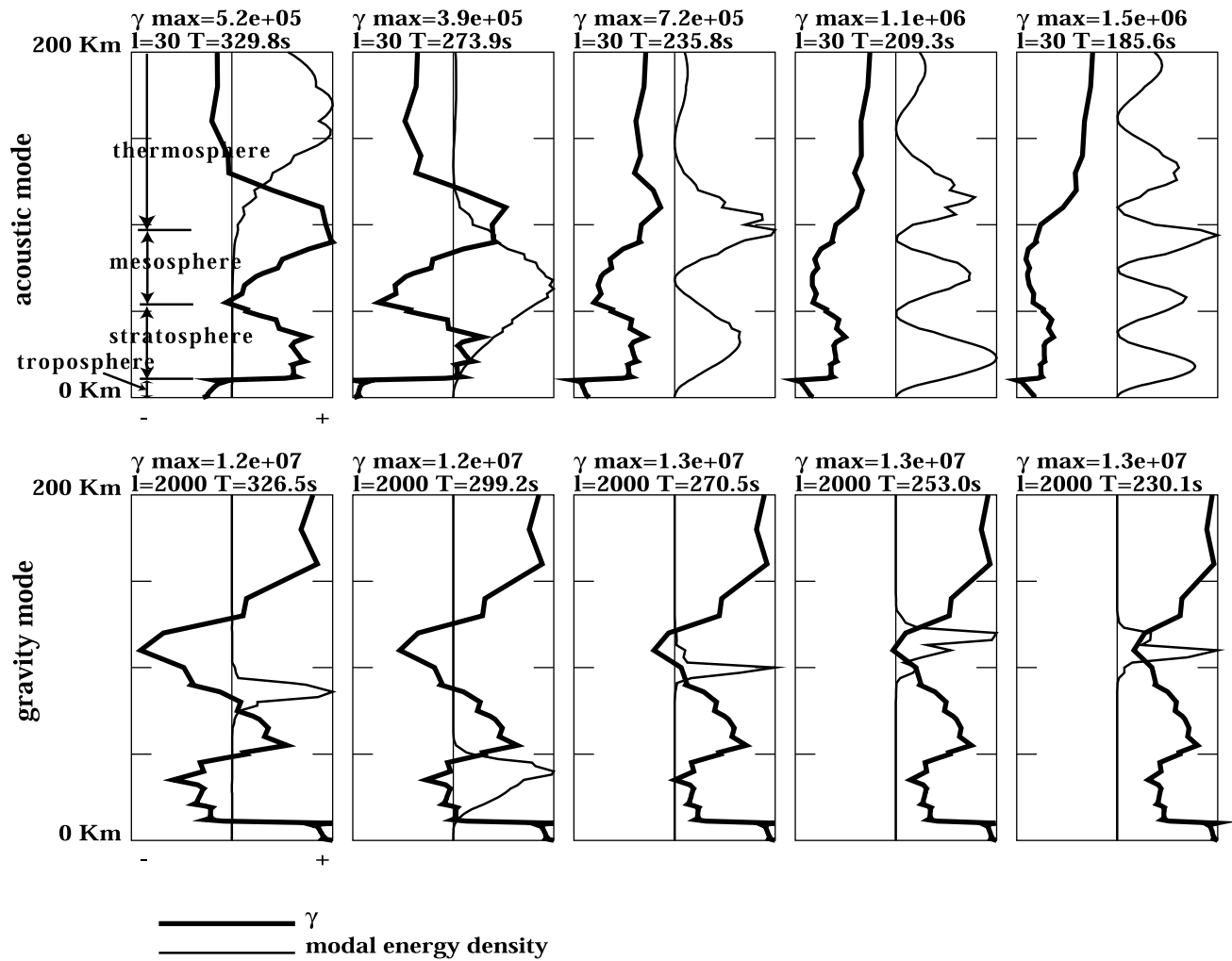


Figure 4. Modal energy density $\rho_o (|U|^2 + l(l + 1)|V|^2)r^2$ of acoustic modes $l = 30$ (equivalent horizontal wavelength ~ 1300 km) and gravity modes $l = 2000$ (equivalent horizontal wavelength ~ 20 km) with a period of about 230 ~ 330 s with a free surface boundary condition. The local characteristic function γ in equation (33) is computed as a function of radius for the eigenperiod and angular order of each mode. Here $\gamma > 0$ is seen as a potential wall where modal energy evades and the eigenfunction becomes evanescent. Here $\gamma < 0$ is seen as a potential well where modal energy is trapped. The modal energy for each mode is normalized to the maximum value. Here γ is also normalized to its maximum. The scale for γ is at the top, but the unit is arbitrary.

A notable feature in Figure 6 is the tsunami branch with a nearly constant horizontal phase velocity of about 170 m/s. This mode is a surface gravity wave in the top ocean layer of the PREM earth model with a thickness of $h = 3$ km. The tsunami branch and seismic branches are separated well in the (frequency order number) domain (Figure 6). For the tsunami mode a simple long-wave approximation gives a nondispersive horizontal phase velocity $\sqrt{g_o h}$ which is close to the horizontal phase velocity of the tsunami modes computed for PREM. At very long wavelength, the horizontal phase velocity slightly decreases. For example, at $l = 10$ the horizontal phase velocity decreases by about 3% from 170 m/s. At long period the Coriolis effect should be taken into account. At short wavelength, the dispersion relation of water waves deviates from the shallow water approximation and approaches the deep water approximation, and its horizontal phase velocity decreases according to

$\sqrt{g_o/k_h}$. The reason why the two waves, Rayleigh waves and tsunamis with similar eigenfrequencies, do not couple efficiently is that the wavelength of the excess pressure field at the ocean bottom caused by tsunamis is different from the wavelength of Rayleigh waves by more than an order of magnitude. Two waves having an interface between them are able to couple efficiently when both the period and the horizontal wavelength of the two waves are the same. This computation confirms the study by Comer [1984] who showed that for a flat earth model, Rayleigh waves and tsunamis are practically uncoupled over the entire periods of seismic waves, and the elasticity of the Earth can be safely ignored for computation of tsunami. This weak coupling between seismic surface waves and tsunamis explains why the tsunamis in the ocean are reported as a loading source of forced deformation of the Earth's surface [Yuan *et al.*, 2005], but never reported as a distinct excitation source of

variation of eigenperiod of Earth atmosphere

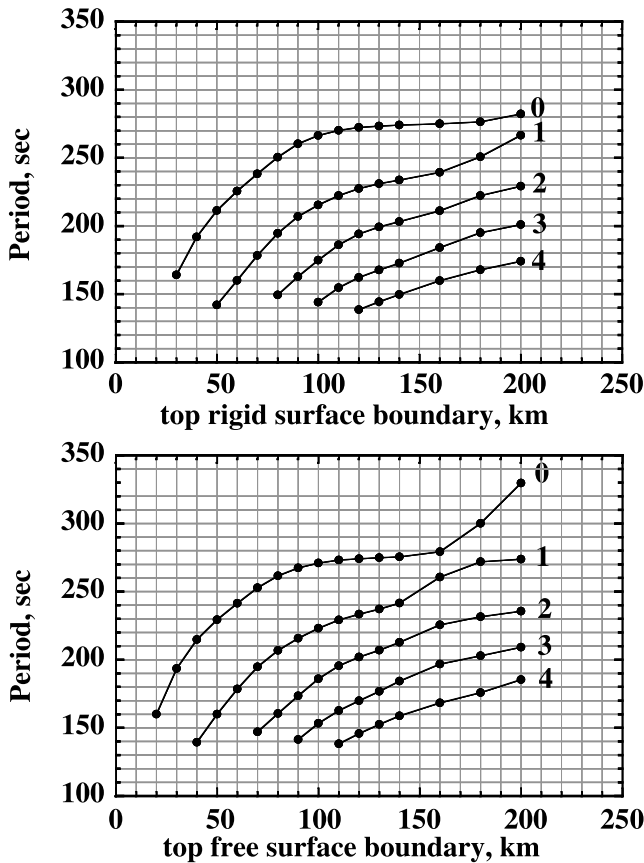


Figure 5. The variation of the eigenperiod of atmospheric acoustic modes ($l = 30$) for the altitude change of the top boundary. The number of each line is the overtone index number. (top) For rigid surface boundary. (bottom) For free surface boundary. Long-wavelength atmospheric acoustic modes tend to have a natural eigenperiod of 270 s. The natural eigenperiod is irrelevant to the top boundary types and the altitudes of the imposed top boundary.

surface waves of the solid earth. However, it should be noted that tsunamis are indeed excited by the local deformation at the ocean bottom associated with earthquakes. In this case the initial disturbance of tsunami is caused by a sudden uplift or subsidence of the ocean surface displaced from a gravitational equipotential surface and is not related to the wave coupling.

[38] The adoption of the Cowling approximation changes the eigenperiod of the nonradial spheroidal normal modes. The eigenperiods of the fundamental spheroidal modes with and without the Cowling approximation for a solid earth model are shown in Table 3. The frequency of fundamental spheroidal modes which we are interested in, 3–5 mHz or 333–200 s, changes by less than 0.3%. The merit of the use of the Cowling approximation is that we can reduce the computational time and improve the computational accuracy because we have fewer dependent variables. The Cowling approximation is used for the large angular order gravity wave modes which become unstable easily. Acoustic and Lamb wave modes are computed without the Cowling

Table 2. Comparison of the Eigenmodes of the Two Atmospheric Models^a

Mode Type	Period (s)	
	Standard Atmosphere	Local at Mt. Pinatubo
acoustic	274	272
acoustic	236	235
acoustic	209	207
acoustic	186	182
gravity	299	320, 290

^aU.S. Standard Atmosphere [1976] and local model near Mt. Pinatubo atmosphere in Figure 1. The same boundary conditions used in Figure 2 are applied. Acoustic mode with $l = 30$ and gravity mode with $l = 2000$ are computed.

approximation. If we take the radiation boundary condition, we used the Cowling approximation for all types of modes.

5. Resonance Mechanism Between the Atmosphere and the Solid Earth

[39] The acoustic coupling between the atmosphere and the solid earth has been considered to be very small. The atmosphere is treated as a vacuum by seismologists and the surface of the Earth is a rigid boundary for atmospheric scientists because of the large acoustic impedance contrast; $(\rho c)_{atmosphere}/(\rho c)_{crust}$ is about the order of 10^{-4} . The horizontal phase velocity of acoustic waves in the atmosphere differs from that of seismic waves by 1 order of magnitude. However, in a few cases ground motions induced by the atmospheric acoustic coupling at a period of seismic normal modes have been observed on seismograms. Seismic waves with a period of about 240 s excited by the pressure pulse near a nuclear explosion in the air were observed by a ground tiltmeter [Ben-Menahem and Singh, 1981] at a teleseismic distance. Harkrider et al. [1974] computed theoretical seismograms from atmospheric point sources for the funda-

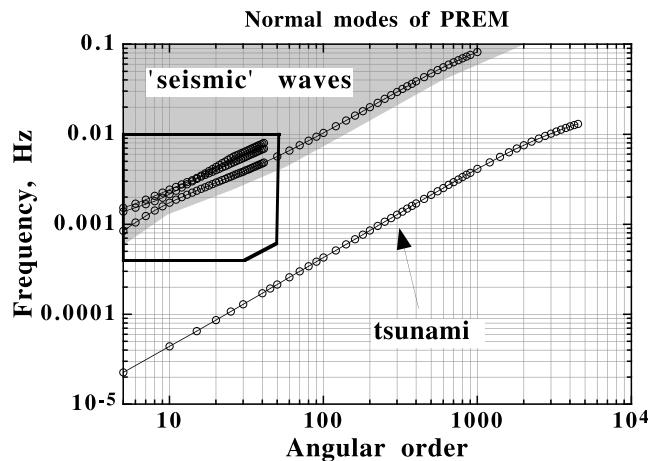


Figure 6. Spheroidal normal modes in the PREM [Dziewonski and Anderson, 1981] earth model which has a 3 km ocean layer at the top that allows water waves. Seismic waves and tsunami waves are almost decoupled. High angular order normal modes $l > 50$ and tsunami modes are computed using the Cowling approximation. The boxed region is magnified in Figure 7.

Table 3. Eigenperiod of Fundamental Spheroidal Modes for the PREM Earth Model in s^a

Angular Order	Cowling Approximate ^b	Exact ^c
2	4127.43	3233.51
3	2505.96	2134.26
4	1693.90	1545.43
5	1258.02	1189.87
6	999.04	963.18
7	832.87	811.81
8	720.92	707.45
9	642.86	633.59
10	586.01	579.21
11	542.21	536.93
12	506.63	502.41
13	476.76	473.27
14	451.05	448.14
15	428.65	426.18
16	408.93	406.79
17	391.38	389.54
18	375.68	374.06
19	361.52	360.10
20	348.68	347.41
21	336.95	335.82
22	326.20	325.17
23	316.25	315.33
24	307.04	306.19
25	298.43	297.67
26	290.39	289.69
26	290.39	289.69
27	282.84	282.19
28	275.71	275.12
29	268.98	268.43
30	262.60	262.08
31	256.53	256.05
32	250.76	250.31
33	245.24	244.82
34	239.97	239.58
35	234.93	234.56
36	230.09	229.75
37	225.45	225.13
38	220.99	220.69
39	216.71	216.42
40	212.58	212.31
41	208.60	208.34
42	204.76	204.52
43	201.06	200.84
44	197.49	197.27
45	194.04	193.83
46	190.70	190.51
47	187.47	187.29
48	184.34	184.17
49	181.32	181.15
50	178.39	178.23

^aThe physical dispersion is included in both cases.

^bIgnores the gravity potential perturbation but includes the reference gravity.

^cIncludes the effect of self gravity.

mental Rayleigh waves with a period of less than 60 s at teleseismic distances. Long-period harmonic Rayleigh wave motion associated with the 1991 eruption of Mt. Pinatubo (15.14°N 120.35°E) in the Philippines, were reported by *Kanamori and Mori* [1992] and *Widmer and Zürn* [1992], and with the 1982 El Chichón eruption by *Widmer and Zürn* [1992] (Table 1).

[40] We can expect efficient coupling between the solid earth and the atmosphere if seismic modes and the atmospheric modes fall into the same region of the frequency-wavenumber ($\omega - k$) domain. In fact, a common region of atmospheric modes and seismic modes exists near the period

of about 200 ~ 300 s (Figure 7), the period of the observed Rayleigh waves. As discussed in section 3, an atmospheric acoustic mode near the period 200 ~ 300 s with a small angular order has a small horizontal group velocity and the modal energy density is trapped in the atmosphere below the thermosphere. Once a long-wavelength atmospheric acoustic mode is excited by a point source in the air, the modal energy is confined in the atmosphere horizontally and vertically. The trapped acoustic mode can efficiently excite a Rayleigh wave that has the same eigenfrequency and horizontal wavelength to those of the acoustic mode.

6. Comparison of Synthetic Ground Motion With Observations

[41] Since the observed surface waves are fundamental mode Rayleigh waves [*Kanamori and Mori*, 1992; *Widmer and Zürn*, 1992], we compute the normal modes near the fundamental spheroidal mode branch (Figure 8) for a spherically symmetric earth model including the ocean and atmosphere. These waves represent seismic Rayleigh waves and acoustic waves in the atmosphere. The normal modes of a coupled system using a combined earth model automatically takes into account the mechanical coupling between the atmosphere, ocean and solid earth. The computed eigenfrequencies for the combined model deviate little from the uncoupled eigenfrequencies except when two modes with the same angular order have very close eigenfrequencies.

[42] The modal energy density of the fundamental spheroidal modes for the combined earth model is shown in Figure 9. Note that the plotted energy density in the atmosphere is magnified by 100. The atmospheric part of the energy density of Rayleigh waves is usually less than 1% of the maximum energy density in the solid earth. Conversely the acoustic modes, which are not shown in Figure 9, also have little energy penetration in the solid earth. For a few exceptional seismic spheroidal modes with a period close to

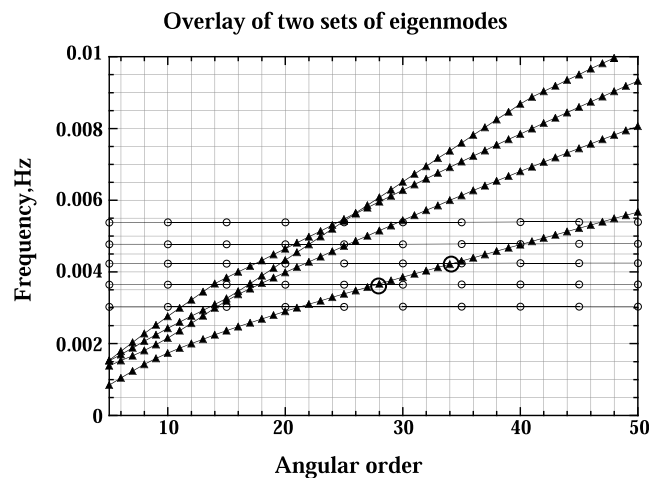


Figure 7. Overlay of atmospheric modes (box in Figure 2) and seismic modes (box in Figure 6). Solid triangles and open circles are fundamental and higher spheroidal modes and atmospheric acoustic modes, respectively. Strong coupling between the Rayleigh waves and the atmospheric acoustic waves is expected at the two bold circles around triangles because of the proximity of the horizontal phase velocities.

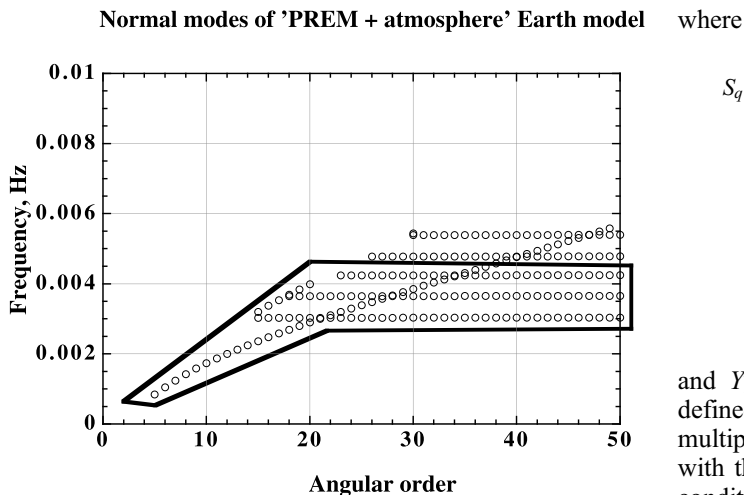


Figure 8. Frequency-angular order plot of normal modes for the combined earth model. Normal modes of the combined PREM earth model and *U.S. Standard Atmosphere* [1976]. Only modes inside the polygon are used in the computation of synthetic spectrum in Figure 11.

the trapped atmospheric acoustic modes, the peak amplitude of the energy density in the atmosphere is as large as 1% of the peak density amplitude in the solid earth. The small but significant modal energy distribution of 272 s and 237 s spheroidal modes in the atmosphere suggests that the 272 s and 237 s modes are preferentially excited by a source in the lower atmosphere compared to other spheroidal modes because the excitation amplitude of an eigenmode by a point source is roughly proportional to the energy density amplitude at the location of the source.

[43] The amplitude in the air of a seismic spheroidal mode can be large because of the very small density in the upper atmosphere. From the ratio of the amplitude peaks of the modal energy density in the air and the solid earth, $\sim 1\%$, and the ratio of material density at the peaks, $\sim 10^{-10}$, we get $u_{\text{at } z=100 \text{ km}}/u_{\text{at } z=-50 \text{ km}} \sim 10^4$. When the mode has an amplitude of $1 \mu\text{m}$ at the ground, the amplitude of this mode at $z = 100 \text{ km}$ is about 1 cm and much smaller than the horizontal wavelength of this mode of about 1000 km or more. At $z = 100 \text{ km}$ the linear amplitude theory of small oscillations is still valid.

[44] We compute the synthetic seismograms using the eigenfunctions for the combined earth model for the subset of modes shown in Figure 8. The excitation source is modeled by an isotropic point source with a moment M_o (three orthogonal dipoles each having a dipole moment of M_o) which is located at $(r_s, 0, 0)$ and varies as a step function in time.

[45] The displacement at (r, θ, φ) in the epicentral coordinates is given by [Woodhouse and Girnius, 1982]

$$u_r(r, \theta, \varphi, t) = \sum_q b_0 U_q(r) Y_l^0(\theta, \varphi) S_q e^{i\omega_k t}, \quad (53)$$

$$u_\theta(r, \theta, \varphi, t) = \sum_q b_1 V_q(r) (-Y_l^1(\theta, \varphi) + Y_l^{-1}(\theta, \varphi)) S_q e^{i\omega_k t}, \quad (54)$$

$$u_\varphi(r, \theta, \varphi, t) = 0, \quad (55)$$

where

$$S_q = -b_0 M_o \left(\frac{\partial U_q(r_s)}{\partial r_s} + \frac{2U_q(r_s)}{r_s} - \frac{l(l+1)V_q(r_s)}{r_s} \right), \quad (56)$$

$$b_0 = \sqrt{\frac{2l+1}{4\pi}}, \quad (57)$$

$$b_1 = \frac{1}{2} \sqrt{\frac{(2l+1)(l+1)l}{4\pi}}, \quad (58)$$

and $Y_l^m(\theta, \varphi)$ are the generalized spherical harmonics defined by *Phinney and Burridge* [1973] and q denotes a multiplet mode. The eigenfunctions used here are computed with the free or zero radial displacement surface boundary condition and normalized by

$$\int_0^R \omega^2 \rho_o (U_q^2 + l(l+1)V_q^2) r^2 = 1. \quad (59)$$

The original broadband seismogram recorded on the day of the Pinatubo eruption is shown in Figure 10. The amplitude spectrum of the synthetic ground motion is plotted in Figure 11. As we expected, the spheroidal modes near 270 s and 230 s are preferentially excited and the observed amplitude ratio of the two peaks near 230 s and 270 s is reproduced in the synthetic. We did not include the modes with periods shorter than 200 s because in the real Earth, the atmospheric eigenfunction becomes a propagating acoustic wave (section 3) and the excitation of the mode by a source in the propagating region will be small compared to the excitation by a source in the standing wave region. We have not used a normal mode approach to compute synthetics for the radiation boundary condition as proposed by *Yamamura and Kawakatsu* [1998].

[46] A higher-altitude source yields larger ground motion because the energy density of the strongly coupled modes (230s and 270s) increases with altitude in the troposphere and the stratosphere (up to 50 km) and these modes are excited more efficiently by a source at higher altitude. In our synthetic experiments, the amplitudes of the ground motion excited by a source located at 1, 2, 4 and 8 km in the air relative to those excited by a source at 0.5 km, are 1.1, 1.2, 1.5 and 2.2, respectively. The waveforms of harmonic oscillations have little dependence on the source altitude.

[47] Seismic moment has been used to express the magnitude of earthquakes in seismology; however, the source description in terms of energy is more appropriate for volcanic eruptions. The volcanic eruption source could be modeled by a non isotropic dipole moment source, for example by a combination of dipoles with different moments, but for simplicity we use an isotropic dipole source in this paper. We consider a small spherical source volume with a radius ϵ around the point source in a fluid. If we use an isotropic dipole moment source the displacement at the surface of the source volume is given by

$$u_\epsilon = \frac{M_o}{4\pi\epsilon^2\kappa}, \quad (60)$$

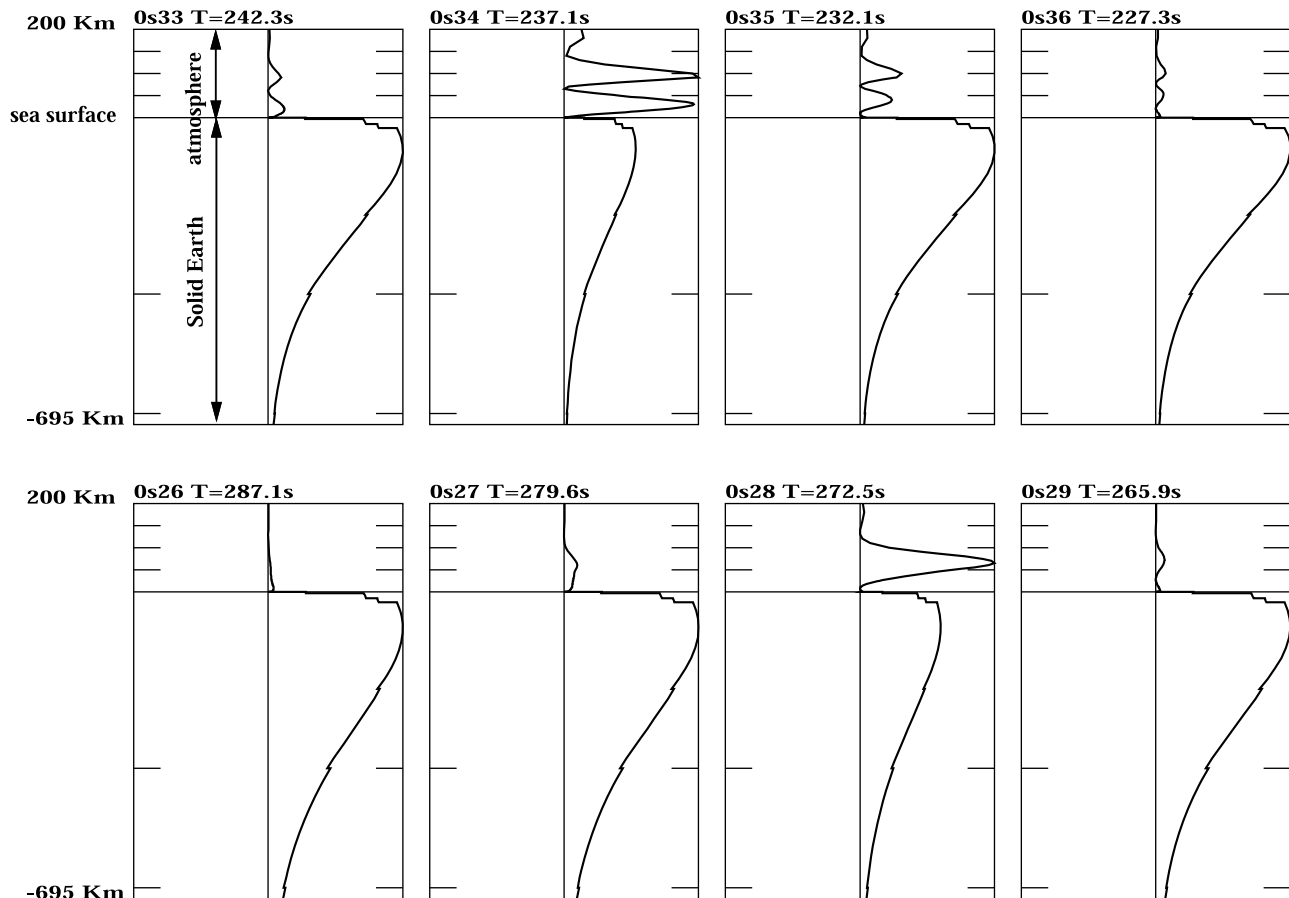


Figure 9. Modal energy density distribution of the fundamental spheroidal modes, from ${}_0S_{26}$ to ${}_0S_{36}$, near the trapped atmospheric acoustic mode branch for the combined earth model. Energy density in the atmosphere is magnified by 100. Amplitude of energy density of each mode is normalized by its maximum value and scale is linear. Note that two spheroidal modes, ${}_0S_{28}$ and ${}_0S_{34}$, which coupled to the atmospheric modes have large modal energy density in the atmosphere.

where κ is the incompressibility. In terms of an energy source, this process can be approximately replaced by an energy source in which a work is done to push the spherical wall at ϵ by u_ϵ against the pressure P_o . Thus, $E_\epsilon = 4\pi\epsilon^2 u_\epsilon P_o$. From these two equations, we obtain $E_\epsilon = P_o M_o/\kappa = M_o/\gamma$, which we will use as a relation between M_o and E_ϵ .

[48] The displacements we compute with equations (53) and (54) are the response to injection of energy given by a step function (i.e., instantaneous injection). In other words, the energy rate is given by a delta function. Thus, the response in the far field to a source for which the energy is injected at a constant rate over a duration of τ can be given by convolving the step function response by a box car function with an amplitude of $1/\tau$ and duration τ . This is equivalent to multiplying the frequency domain step function response by $\sin(\omega\tau/2)/(\omega\tau/2)$. In case of the 1991 Pinatubo eruption, since the source duration is much longer than the period of the observed Rayleigh waves, the effect of the finite source duration is equivalent to diminishing the step function response by a factor $1/\omega\tau$.

[49] Kanamori and Mori [1992] observed that the source duration is at least 2 h. If we take the 2 h as the source duration τ , and the frequency of the resonant period, the

dipole moment 10^{19} Nm is required to explain the Rayleigh wave amplitude. The time domain synthetic waveform looks like an undulating sine wave, just as seen in Figure 10, since the signal power is dominated at two frequencies.

[50] Based on the conversion from isotropic moment to energy, we can roughly estimate the energy release from Mt. Pinatubo during the major eruption in 15 June 1991, about $10^{19}/1.4$ J. Using the relationship between the size of a nuclear explosion and its energy release, a one ton nuclear explosion releases 10^9 calories = 4.2×10^9 J (G. D. Harkrider, personal communication, 1995), the energy release during the 1991 Mt. Pinatubo eruption corresponds to a 1700 Mton size nuclear explosion. For a more precise estimate we need to model the physical mechanism of volcanic eruptions, and the excess thermal and mass input should appear in the equation of motion as excitation terms [Pierce, 1968].

7. Discussion

[51] The air-sea coupling, instead of the air-ground coupling discussed in this paper, was studied by Press and Harkrider [1966] and Harkrider and Press [1967]. They discussed the coupling between the ocean waves and the

Observation

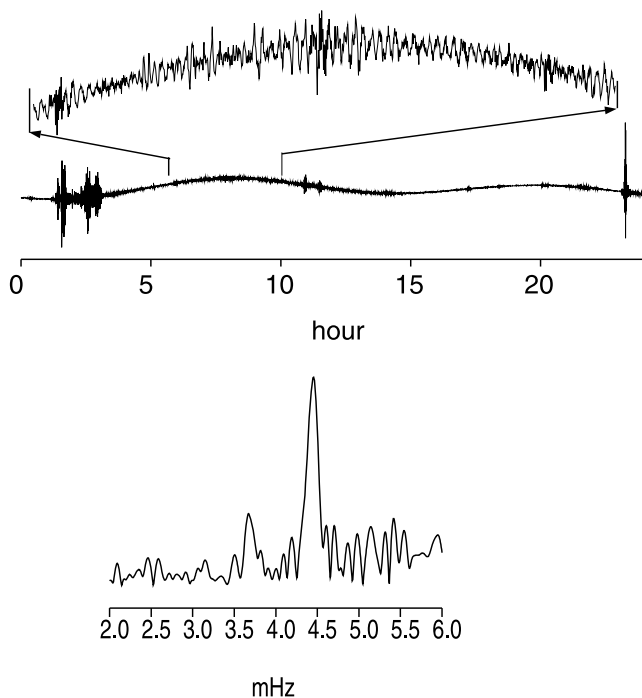


Figure 10. (top) Observed harmonic signals in vertical very long period channel data at MAJO ($\Delta = 26^\circ$) Matsushiro, Japan. The record starts at 15 June 1991 0000 UT. The large signals in the first 5 h are from teleseismic events, a Ms 6.5 in the Caucasus and a Ms 6.5 in the South Sandwich Island. The peak to peak amplitude is about $6 \mu\text{m}$ after removing the very long period tidal signals. (bottom) Amplitude spectra of the magnified part of the seismogram. The peaks at 4.4 mHz (230 s) and 3.7 mHz (270 s) are observed at many seismographic stations. The vertical scale is linear.

atmospheric internal gravity waves excited by the 1883 Krakatoa eruption. They showed that in the synthetic margram computed for a source in the air, three distinct signals corresponding to the Lamb wave branch, an internal gravity wave branch and the tsunami branch exist; however, in the synthetic barograph only two signals corresponding to the first two air waves appear and no substantial signal exists at the arrival time of the tsunami wave. If we consider only the static pressure response of the ocean surface for the surface atmospheric pressure loading and unloading originating from a source in the air, the missing atmospheric pressure disturbance corresponding to the tsunami is not explained. In Figure 2b, if we draw a dispersion line of long waves in the ocean, tsunami, with a constant horizontal phase velocity of about 170 m/s as we do in Figure 6, the tsunami branch crosses the internal gravity mode branches of the atmosphere. The ocean dynamic response for an atmospheric pressure disturbance is frequency dependent and becomes very sensitive to a wave in the atmosphere which has the same wavelength and period as that of tsunami. Those

atmospheric waves with a very small pressure amplitude couple to the ocean and explain the tsunami without a corresponding pressure disturbance.

[52] The mechanism of the coupling of the atmospheric acoustic modes to the solid earth, that we discussed earlier, is similar to this case. In both cases, two media, one overlaying the other, sustain waves with the same wavelength and frequency along the boundary. The coupling sometimes becomes so strong that we only observe the waves in the layer which does not contain the source. For the 1883 Krakatoa eruptions, the source is in the air, atmospheric waves were excited, and the waves in the ocean layer, tsunami, were excited through air-sea coupling. For the 1991 Pinatubo eruption, the source is also in the air, atmospheric waves are also excited, and the waves in the solid earth, Rayleigh waves, were excited through air-ground coupling.

[53] Wind is not included in our computational scheme. Wind changes the apparent phase velocity of the atmospheric waves. For the atmosphere-solid earth coupling, the horizontal phase velocity of the acoustic modes coupled to the Rayleigh waves is about the seismic surface wave speed which is at least 2 orders of magnitude faster than the wind speed. We suspect that inclusion of the wind effect will not significantly change our results.

[54] In our modal computation in the atmosphere we have neglected viscosity. Below $z \approx 100$ km the kinetic eddy viscosity has about constant value $\sim 100 \text{ m}^2/\text{s}$ and the molecular viscosity is several orders of magnitude smaller. At $z \approx 200$ km the atmospheric density decreases further to about 10^{-10} of the surface air density, or 10^{-3} of

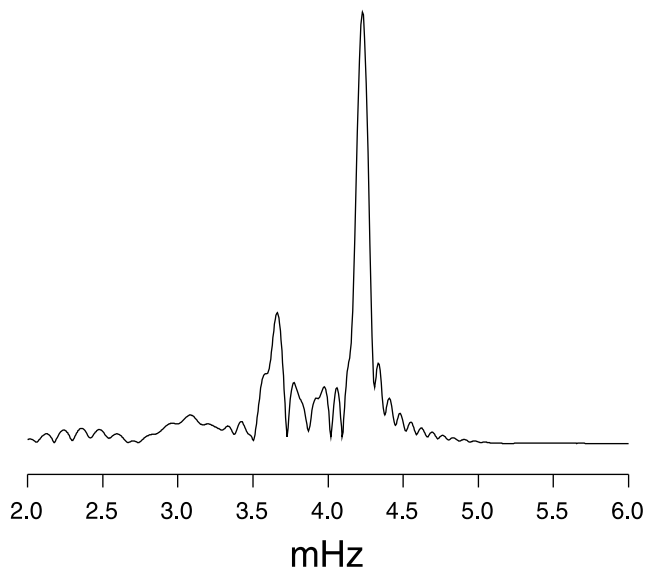


Figure 11. Fourier amplitude spectrum of the synthetic ground motion at MAJO for a point source located 1 km high in the atmosphere. The ground motion is computed using the normal mode method by summing up the modes in Figure 7. A dipole moment of $7 \times 10^{18} \text{ Nm}$ is required to explain the observed ground motion for a 2 h long source duration. The amplitude spectra is computed for a 4.4 h long synthetic seismogram starting at 45 min after the origin time. The vertical scale is linear.

the air density at $z \approx 100$ km. Above $z \approx 100$ km the molecular diffusion is the dominant factor in the dissipation of atmospheric waves, and its value increases with altitude [U.S. Standard Atmosphere, 1976]. If waves going through the viscous region, wave energy is dissipated. The difference between eigenfunctions below the highly viscous region ($z > 100$ km) for different types of the upper boundary condition will be small and the top boundary condition becomes less important [Francis, 1973]. The dissipation of a seismic spheroidal mode resulting from the wave dissipation in the atmosphere is negligible compared to the dissipation due to intrinsic attenuation in the solid earth because the total energy in the atmosphere is only a very small fraction of the total modal energy of the spheroidal mode.

[55] In this paper, two periods of bichromatic ground motion are interpreted to be a result of resonance between the solid earth Rayleigh waves and the acoustic mode of the atmosphere near and above the the acoustic cutoff period. Kanamori and Mori [1992] and Kanamori et al. [1994] initially interpreted the 230 s and 270 s modes excited by the Pinatubo eruption as the acoustic and gravity mode, respectively. However, in the stratified atmosphere of the Earth, the acoustic mode has the gravest mode (270 s) and overtones (230 s) trapped below the thermosphere, and both the 230 s and 270 s modes are acoustic modes. Later, Kanamori [2004] corrected the earlier interpretation. Gravity modes do not couple to seismic waves because of the large impedance mismatch and large difference of wavelength and period at the Earth's surface, but they can be observed with a barograph as shown for the 1980 Mt. St. Helens eruption and the 1883 Krakatoa eruption.

[56] Resonant phenomena were also detected as large amplitude anomalies of the continuous oscillations of the Earth by Nishida et al. [2000] near the frequencies of 270 s and 230 s. The observed modal amplitude of these modes are about 10 or 20% larger than those of the adjacent fundamental spheroidal modes of the solid earth. This situation is different from that for the 1991 Mt. Pinatubo eruption for which the amplitudes of coupled and uncoupled modes are very different (Figure 10). The less conspicuous amplitude anomaly of the resonant modes observed in the continuous oscillations of the Earth hints that the excitation mechanism of the continuous oscillations of the Earth is somewhat different from the point source description we have used for the eruption of Mt. Pinatubo. If we put a point isotropic source in the atmosphere in synthetic simulations, even at the lowest level, the coupled modes are excited well relative to the uncoupled modes and inevitably exhibit significant amplitude anomalies (Figure 11). These arguments suggest that, since atmospheric turbulence causes ground surface loading as well as Reynolds stress in the air that is equivalent to distributed point sources in the atmosphere, seeking direct excitation sources of the continuous oscillations of the Earth in the atmospheric turbulence [Tanimoto, 1999; Fukao et al., 2002] seems unwarranted.

8. Conclusion

[57] The two peaks at about 230 and 270 s of the amplitude spectra of the ground motion observed for the 1991 Mt. Pinatubo eruption correspond to the resonant period

of very long wavelength standing acoustic modes in the atmosphere. For a standard atmosphere and solid earth model, a few atmospheric acoustic modes at low angular order numbers become a standing wave in the atmosphere and have the same eigenperiod of the spheroidal modes (${}_0S_{28}$, ${}_0S_{34}$) of the solid earth with the same horizontal wavelength. These acoustic modes in the air, set off by the volcanic eruption, can couple to Rayleigh waves efficiently. The oscillation of the standing acoustic waves selectively excites Rayleigh waves which are detected with seismographs at teleseismic distances. On the other hand, the gravity mode with a period of 300 s was recorded as a barographic pressure change near a volcanic source such as the 1980 Mt. St. Helens eruption, but was not detected by seismographs. Because of its slow horizontal phase velocity of about 10 m/s, the gravity wave does not couple to Rayleigh waves efficiently.

[58] From the energy density distribution and the local behavior analysis of the normal modes of the atmosphere, we found that the atmospheric structure near the mesopause and the thermosphere results in a standing acoustic wave with long wavelength confined between the ground and the thermosphere. The mode with a period of 270 s is the gravest mode for this structure and the mode with a period of 230 s is the first overtone. Higher overtones become vertically propagating waves and will not be a source of harmonic loading on the surface. The gravity mode with a period of 300 s is a trapped mode in the stratosphere. A regional or temporal variation of the atmospheric structure, such as lower temperature in the stratosphere in the tropics and higher thermospheric temperature caused by the high solar activity, may result in variations of the period of the barographic oscillations. The eigenperiod of the gravity mode trapped in the stratosphere will change. Also there can be an additional mode in the harmonic ground motion due to the appearance of the second standing overtone.

[59] To simulate the coupling effect between the atmosphere and the solid earth during the volcanic eruption of Mt. Pinatubo, synthetic ground motion is computed with the normal mode method. The observed amplitude spectral peaks of long-period Rayleigh waves at 230 s and 270 s are seen in the synthetic amplitude spectrum and the amplitude ratio of the two peaks is reproduced in the simulation.

[60] The observed absolute amplitude is explained by an isotropic point source with a dipole moment 10^{19} Nm with a 2 h long source duration. Using the conversion from a moment source to an energy source, the amount of energy, which contributed to the excitation of atmospheric waves, released from the 15 June 1991 Mt. Pinatubo eruption is estimated at about 7×10^{18} J.

Appendix A: Equation of Motion

[61] To emphasize the Lagrangian approach for the analysis of small oscillations of fluid, in contrast to the Eulerian approach often used in fluid dynamics text books [e.g., Lamb, 1945; Ledoux and Walraven, 1958; Cox, 1980; Unno et al., 1989] we derive the differential equations for a fluid (equation (1)) from the basic physical principles. Note that the equations of motion and the boundary conditions expressed using Lagrangian and Eulerian variables for a small oscillation of an elastic body look different, however,

the equations and the boundary conditions are entirely compatible through equation (A8). The use of Eulerian variables or Lagrangian variables or mixed use of variables is a matter of choice. The dispersion relation which characterizes the relation between wavenumbers and angular frequency should be the same, as long as the small oscillation assumption is valid.

[62] The basic equations that govern the inviscid, adiabatic oscillatory motions of a self-gravitating fluid with a small amplitude are: Linear momentum balance obtained from the linearized Navier–Stokes equation

$$\rho \frac{D^2 \mathbf{u}}{Dt^2} = -\nabla P + \rho \mathbf{g}. \quad (\text{A1})$$

Equation of continuity

$$\delta \rho + \rho \nabla \cdot \mathbf{u} = 0. \quad (\text{A2})$$

The adiabatic equation of state for an ideal fluid

$$\delta \rho = \left(\frac{\partial \rho}{\partial P} \right)_s \delta P = \frac{\delta P}{c^2}. \quad (\text{A3})$$

The Poisson equation for gravitational potential

$$\nabla^2 \phi = 4\pi \rho. \quad (\text{A4})$$

The definition of the gravitational potential

$$\mathbf{g} = -\nabla \phi. \quad (\text{A5})$$

In the above, δ denotes the Lagrangian perturbation which is defined for a given parcel of the medium at \mathbf{x} which was originally at \mathbf{x}_o at rest. In the following, Eulerian perturbation, denoted by $'$ is defined as a perturbation of a physical quantity at a given position \mathbf{x} . A physical quantity $f(\mathbf{x}, t)$ and its reference state $f_o(\mathbf{x})$ are therefore expressed by either

$$f(\mathbf{x}, t) = f_o(\mathbf{x}) + f'(\mathbf{x}, t) \quad (\text{A6})$$

or

$$f(\mathbf{x}, t) = f_o(\mathbf{x}_o) + \delta f(\mathbf{x}, t). \quad (\text{A7})$$

The Lagrangian and Eulerian perturbations are related to each other to the first order of \mathbf{u} by

$$\delta f(\mathbf{x}, t) = f'(\mathbf{x}, t) + \mathbf{u} \cdot \nabla f_o(\mathbf{x}) \quad (\text{A8})$$

and by

$$\mathbf{x} = \mathbf{x}_o + \mathbf{u}, \quad (\text{A9})$$

$$\frac{D}{Dt} = \frac{\partial}{\partial t} + \mathbf{v} \cdot \nabla, \quad (\text{A10})$$

where \mathbf{v} is the Lagrangian velocity of the material element.

[63] Subtracting the reference equations such as

$$-\nabla P_o + \rho_o \mathbf{g}_o = 0, \quad (\text{A11})$$

$$\nabla^2 \phi_o = 4\pi \rho_o, \quad (\text{A12})$$

and

$$\mathbf{g}_o = -\nabla \phi_o = -g_o(r) \hat{r}, \quad (\text{A13})$$

where $\mathbf{g}_o = (-g_o(r), 0, 0)$ in the spherical coordinates (r, θ, φ) , and ignoring the second order of the displacement and perturbations, we obtain the equation of motion of the perturbed states

$$\rho_o \frac{\partial^2 \mathbf{u}}{\partial t^2} + \nabla P' + \rho' \mathbf{g}_o \hat{r} + \rho_o \nabla \phi' = 0, \quad (\text{A14})$$

$$\delta \rho + \rho_o \nabla \cdot \mathbf{u} = \rho' + \nabla \cdot (\rho_o \mathbf{u}) = 0, \quad (\text{A15})$$

$$\delta \rho = \frac{\delta P}{c^2}, \quad (\text{A16})$$

$$\nabla^2 \phi' = 4\pi G \rho'. \quad (\text{A17})$$

Because $\delta P = P' + \mathbf{u} \cdot \nabla P_o = P' - u_r \rho_o g_o$ and $\rho' = \delta \rho - u_r \frac{d\rho}{dr}$, the radial component of equation (A14) becomes

$$\rho_o \frac{\partial^2 u_r}{\partial t^2} + \frac{\partial \delta P}{\partial r} + \frac{g_o}{c^2} \delta P + \rho_o \frac{d(u_r g_o + \phi')}{dr} = 0. \quad (\text{A18})$$

We should note that δP is a Lagrangian variable and ϕ' is an Eulerian variable, the equation of motion is not called an Eulerian equation nor a Lagrangian equation. Two types are mixed into a single equation. Two variables are at \mathbf{x}_o at rest, but in motion measured at different locations at \mathbf{x} and \mathbf{x}_o .

[64] In spherical coordinates a vector spherical component (l, m) of the displacement \mathbf{u} can be expressed as

$$\mathbf{u} = (U \hat{r} + \nabla_{\perp} V - \hat{r} \times \nabla_{\perp} W) Y_l^m(\theta, \varphi) e^{i\omega t}, \quad (\text{A19})$$

where

$$\nabla_{\perp} = \left(0, \frac{\partial}{\partial \theta}, \frac{1}{\sin \theta} \frac{\partial}{\partial \varphi} \right) \quad (\text{A20})$$

and $Y_l^m(\theta, \varphi)$ is the spherical harmonic function [e.g., *Arfken*, 1985]. Because from equations (A14)–(A17) we find that the displacement $(\hat{r} \times \nabla_{\perp} W)$ does not result in any pressure, density and potential perturbations, the (l, m) component of the displacement is simply expressed at frequency ω as

$$\mathbf{u}(r, \theta, \varphi, t) = \left(U, V \frac{\partial}{\partial \theta}, \frac{V}{\sin \theta} \frac{\partial}{\partial \varphi} \right) Y_l^m(\theta, \varphi) e^{i\omega t} \quad (\text{A21})$$

and the Lagrangian pressure perturbation as

$$\delta P(r, \theta, \varphi, t) = Q Y_l^m(\theta, \varphi) e^{i\omega t} \quad (\text{A22})$$

and the Eulerian gravitational perturbation as

$$\phi'(r, \theta, \varphi, t) = \Phi Y_l^m(\theta, \varphi) e^{i\omega t}, \quad (\text{A23})$$

where $U(r)$, $V(r)$, $Q(r)$ and $\Phi(r)$ are functions of r . Equation (A18) is written as

$$\left(-\omega^2 \rho_o U + \frac{dQ}{dr} + \frac{g_o}{c^2} Q + \rho_o \frac{d(Ug_o + \Phi)}{dr}\right) Y_l^m(\theta, \varphi) e^{i\omega t} = 0. \quad (\text{A24})$$

By rewriting $\delta P = -c^2 \rho_o \nabla \cdot \mathbf{u}$ and using

$$\nabla \cdot \mathbf{u} = \left(\frac{1}{r^2} \frac{d(r^2 U)}{dr} - l(l+1) \frac{V}{r}\right) Y_l^m(\theta, \varphi) e^{i\omega t}, \quad (\text{A25})$$

we obtain

$$Q = -\kappa \left(2 \frac{U}{r} + \frac{dU}{dr} - l(l+1) \frac{V}{r}\right), \quad (\text{A26})$$

where $\kappa = \rho_o c^2$ is the bulk modulus. The horizontal component of equation (A14) is written as

$$\left(-\omega^2 \rho_o V + \frac{1}{r} (Q + U \rho_o g_o + \rho_o \Phi)\right) \nabla_{\perp} Y_l^m(\theta, \varphi) e^{i\omega t} = 0. \quad (\text{A27})$$

From equations (A15) and (A17) we have

$$\nabla^2 \phi' = -4\pi G (\mathbf{u} \cdot \nabla \rho_o + \rho_o \nabla \cdot \mathbf{u}) \quad (\text{A28})$$

or

$$\frac{d^2 \Phi}{dr^2} + \frac{2d\Phi}{r dr} - l(l+1) \frac{\Phi}{r^2} = -4\pi G \left(\rho_o \left(\frac{dU}{dr} + \frac{2U - l(l+1)V}{r} \right) + U \frac{d\rho_o}{dr} \right). \quad (\text{A29})$$

Introducing a new dependent variable defined as

$$Y_6 = \frac{d\Phi}{dr} + (l+1) \frac{\Phi}{r} + 4\pi G \rho_o U, \quad (\text{A30})$$

we can eliminate V from equations (A26) and (A31). The results are

$$\frac{dU}{dr} = \left(-\frac{2}{r} + \frac{l(l+1)g_o}{\omega^2 r^2}\right) U + \left(-\frac{1}{\kappa} + \frac{l(l+1)}{\omega^2 \rho_o r^2}\right) Q + \frac{l(l+1)}{\omega^2 r^2} \Phi, \quad (\text{A33})$$

$$\frac{dY_6}{dr} = 4\pi G \left(-\frac{(l+1)\rho_o}{r} + \frac{l(l+1)\rho_o g_o}{\omega^2 r^2}\right) U + 4\pi G \frac{l(l+1)}{\omega^2 r^2} Q + 4\pi G \frac{l(l+1)\rho_o \Phi}{\omega^2 r^2} + \frac{(l-1)Y_6}{r}. \quad (\text{A34})$$

From the definition of Y_6 ,

$$\frac{d\Phi}{dr} = -4\pi G \rho_o U - \frac{l+1}{r} \Phi + Y_6. \quad (\text{A35})$$

From equations (A12) and (A13) we find that the reference gravity and density are related by

$$\frac{dg_o}{dr} = 4\pi g_o \rho_o - \frac{2}{r} g_o. \quad (\text{A36})$$

By eliminating $\frac{dU}{dr}$, $\frac{dg_o}{dr}$ and $\frac{d\Phi}{dr}$ from equation (A24), we obtain

$$\frac{dQ}{dr} = \left(\omega^2 \rho_o - \frac{l(l+1)}{\omega^2 r^2} \rho_o g_o^2 + 4 \frac{\rho_o g_o}{r}\right) U - \frac{l(l+1)g_o}{\omega^2 r^2} Q + \left(-\frac{\rho_o g_o l(l+1)}{\omega^2 r^2} + \frac{l+1}{r}\right) \Phi - \rho_o Y_6. \quad (\text{A37})$$

The redefined variables $Y_1 = U$, $Y_2 = -Q$, $Y_5 = \Phi$ and Y_6 are then the same variables defined by *Takeuchi and Saito* [1972] except that the sign of the potential perturbation is opposite. The four simultaneous first-order differential equations (equations (A33), (A34), (A35) and (A37))

$$\frac{d}{dr} \begin{pmatrix} Y_1 \\ Y_2 \\ Y_5 \\ Y_6 \end{pmatrix} = \mathbf{B} \begin{pmatrix} Y_1 \\ Y_2 \\ Y_5 \\ Y_6 \end{pmatrix}, \quad (\text{A38})$$

where B_{ij} 's are given by

$$\begin{pmatrix} \frac{2}{r} + \frac{l(l+1)g_o}{\omega^2 r^2} & \frac{1}{\kappa} - \frac{l(l+1)}{\omega^2 \rho_o r^2} & \frac{l(l+1)}{\omega^2 r^2} & 0 \\ -\omega^2 \rho_o + \frac{l(l+1)}{\omega^2 r^2} \rho_o g_o^2 - 4 \frac{\rho_o g_o}{r} & -\frac{l(l+1)g_o}{\omega^2 r^2} & \frac{\rho_o g_o l(l+1)}{\omega^2 r^2} - \frac{l+1}{r} & \rho_o \\ -4\pi G \rho_o & 0 & -\frac{l+1}{r} & 1 \\ 4\pi G \left(-\frac{(l+1)\rho_o}{r} + \frac{l(l+1)\rho_o g_o}{\omega^2 r^2}\right) & -4\pi G \frac{l(l+1)}{\omega^2 r^2} & 4\pi G \frac{l(l+1)\rho_o}{\omega^2 r^2} & \frac{(l-1)}{r} \end{pmatrix} \quad (\text{A39})$$

equation (A29) is expressed as

$$\frac{dY_6}{dr} = \frac{1}{r} (-(l+1)4\pi G \rho_o U + l(l+1)4\pi G \rho_o V + (l-1)Y_6). \quad (\text{A31})$$

Using V from equation (A27)

$$V = \frac{1}{\omega^2 \rho_o r} (Q + \rho_o g_o U + \rho_o \Phi), \quad (\text{A32})$$

are the governing equations of eigenfunctions in a fluid region [*Takeuchi and Saito*, 1972]. Further, we change the dependent variables from Y_i 's to Z_i 's by

$$Z_1 = rY_1 = rU, \quad (\text{A40})$$

$$Z_2 = rY_2 = -rQ, \quad (\text{A41})$$

$$Z_5 = rY_5 = r\Phi, \quad (\text{A42})$$

$$Z_6 = \frac{rY_6}{4\pi G} = \frac{1}{4\pi G} \left(r \frac{d\Phi}{dr} + (l+1)\Phi \right) + \rho_o r U. \quad (\text{A43})$$

Then the coefficient matrix in equation (A39) is transformed into the one in equation (2). The system of the differential equations improves its symmetry and, together with appropriate boundary conditions, becomes self adjoint [Saito, 1988; Woodhouse, 1988].

Notation

- x^\dagger complex conjugate of variable x .
- $|x|^2$ xx^\dagger .
- ρ, P density and pressure.
- ρ_o, P_o reference atmosphere density and pressure.
- ρ', P' Eulerian perturbation of ρ_o and p_o .
- $\delta\rho, \delta P$ Lagrangian perturbation of ρ_o and p_o .
- r, θ, φ spherical coordinates.
- $(\hat{r}, \hat{\theta}, \hat{\varphi})$ unit vectors in the spherical coordinates.
- t time.
- x local horizontal coordinate.
- z altitude from ground surface or sea surface.
- r_s excitation source location.
- a, b_o, b_1 constants.
- c sound velocity.
- l, m angular and azimuthal orders of the spherical harmonic function.
- c_1 nondimensional density defined by equation (7).
- A^* nondimensional buoyancy frequency defined by equation (27).
- A_{ij} coefficient matrix element of differential equation (2).
- B_{ij} coefficient matrix element of differential equation (A39).
- C_{ij} coefficient matrix element of differential equation (20).
- E modal energy density defined by equation (30).
- E_c energy radiated from an explosive source in the atmosphere.
- \mathbf{F} energy flux vector.
- G gravitational constant.
- \mathbf{g} gravity vector.
- g_o reference gravity acceleration.
- h ocean depth.
- H_s scale height defined by equation (4).
- K nondimensional radius defined by equation (21).
- k_h, k_r horizontal and radial wavenumber.
- k_x, k_z wavenumber in (x,z) direction.
- M_o seismic moment.
- M_r total mass inside radius r .
- N buoyancy frequency.
- N_A acoustic cutoff frequency.
- Q pressure eigenfunction.
- R radius where top boundary is placed.
- S_q earthquake source vector of mode q .
- U vertical displacement eigenfunction.
- U_m nondimensional density defined by equation (5).
- V, W horizontal displacement eigenfunctions.
- V_g nondimensional sound velocity defined by equation (6).
- \mathbf{u} displacement vector.
- \mathbf{v} velocity vector of a material element.
- Y_l^m generalized spherical harmonics used in equations (53) and (54).

- Y_l^m spherical harmonics used in Appendix A.
- Y_i eigenfunctions used in equation (A38).
- Z_i a set of eigenfunctions modified from Y_i (equations (A40)–(A43)).
- X_i a set of eigenfunctions modified from Z_i (equations (17) and (18)).
- ϕ gravitational potential.
- ϕ' Eulerian gravitational potential perturbation.
- Φ gravity potential eigenfunction.
- γ local characteristic function of a mode defined by equation (25).
- Γ specific heat ratio defined by equation (14).
- κ bulk modulus, incompressibility.
- λ local polynomial power term of a mode defined by equation (24).
- ρ density.
- ω angular frequency.
- ω_1 cutoff frequency bounding gravity modes.
- ω_2 cutoff frequency bounding acoustic modes.
- σ nondimensional frequency of ω .
- σ_1 nondimensional frequency of ω_1 .
- σ_2 nondimensional frequency of ω_2 .
- τ eruption or seismic source duration.

[65] **Acknowledgments.** We would like to thank many people who helped us clarify the normal mode formulations from the basic physical first principles. D. Anderson, F. Gilbert, R. Hide, A. Ingersoll, G. Masters, J. Woodhouse, and all the participants of the seismolab coffee breaks convinced us that all the normal mode formalism for the Earth, the Sun, stars, tsunami, and the atmosphere can be derived indeed from a common set of first principles and are consistent with each other.

References

- Aki, K., and P. G. Richards (1980), *Quantitative Seismology*, W. H. Freeman, New York.
- Alterman, Z., H. Jarosch, and C. L. Pekeris (1959), Oscillations of the earth, *Proc. R. Soc. London Ser. A*, 252, 80–95.
- Arfken, G. (1985), *Mathematical Methods for Physicists*, 3rd ed., Academic, San Diego, Calif.
- Artru, J., T. Farges, and P. Lognonné (2004), Acoustic waves generated from seismic surface waves: Propagation properties determined from Doppler sounding observation and normal-mode modeling, *Geophys. J. Int.*, 158, 1066–1077.
- Beer, T. (1974), *Atmospheric Waves*, John Wiley, New York.
- Ben-Menahem, A., and S. J. Singh (1981), *Seismic Waves and Sources*, Springer, New York.
- Champion, K. S. W., A. E. Cole, and A. J. Kantor (1985), Standard and reference atmospheres, in *Handbook of Geophysics and Space Environment*, edited by A. S. Jursa, U.S. Air Force Geophys. Lab., Air Force Syst. Command, Natl. Tech. Inf. Serv., Springfield, Va.
- Comer, R. P. (1984), Tsunami generation—A comparison of traditional and normal mode approaches, *Geophys. J. Astron. Soc.*, 77, 29–41.
- COSPAR Working Group IV (Eds.) (1972), *COSPAR International Reference Atmosphere*, Akademie, Berlin.
- Cowling, T. G. (1941), The non-radial oscillations of polytropic stars, *Mon. Not. R. Astron. Soc.*, 101, 367–375.
- Cox, J. P. (1980), *Theory of Stellar Pulsation*, Princeton Univ. Press, Princeton, N. J.
- Dziewonski, A. M., and D. L. Anderson (1981), Preliminary Reference Earth Model, *Phys. Earth Planet. Inter.*, 25, 297–356.
- Francis, S. H. (1973), Acoustic-gravity modes and large-scale traveling ionospheric disturbances of realistic, dissipative atmosphere, *J. Geophys. Res.*, 78, 2278–2301.
- Friedman, J. P. (1966), Propagation of internal gravity waves in a thermally stratified atmosphere, *J. Geophys. Res.*, 71, 1033–1054.
- Fukao, Y., K. Nishida, N. Suda, K. Nawa, and N. Kobayashi (2002), A theory of the Earth's background free oscillations, *J. Geophys. Res.*, 107(B9), 2206, doi:10.1029/2001JB000153.
- Georges, T. M. (Ed.) (1968), *Acoustic-Gravity Waves in the Atmosphere: Final Program*, U.S. Gov. Print. Off., Washington, D. C.

- Gilbert, F. (1980), An introduction to low-frequency seismology, *Proc. Int. Sch. Phys.*, LXXVIII, 41–81.
- Gill, E. A. (1982), *Atmospheric-Ocean Dynamics*, Academic, San Diego, Calif.
- Harkrider, G. D. (1964), Theoretical and observed acoustic-gravity waves from explosive sources in the atmosphere, *J. Geophys. Res.*, 69, 5295–5321.
- Harkrider, G. D., and F. Press (1967), The Krakatoa air-sea waves: An example of pulse propagation in coupled systems, *Geophys. J. Astron. Soc.*, 13, 149–159.
- Harkrider, G. D., C. A. Newton, and E. A. Flinn (1974), Theoretical effect of yield and burst height of atmospheric explosions on Rayleigh wave amplitudes, *Geophys. J. Astron. Soc.*, 36, 191–225.
- Jensen, F. B., W. A. Kupperman, M. B. Porter, and H. Schmidt (1994), *Computational Ocean Acoustics*, AIP Press, New York.
- Kanamori, H. (2004), Some fluid-mechanical problems in geophysics—Waves in the atmosphere and fault lubrication, *Fluid Dyn. Res.*, 34, 1–19.
- Kanamori, H., and J. Mori (1992), Harmonic excitation of mantle Rayleigh waves by the 1992 eruption of Mount Pinatubo, Philippines, *Geophys. Res. Lett.*, 19, 721–724.
- Kanamori, H., J. Mori, and D. G. Harkrider (1994), Excitation of atmospheric oscillations by volcanic eruptions, *J. Geophys. Res.*, 99, 21,947–21,961.
- Kobayashi, N. (2007), A new method to calculate normal modes, *Geophys. J. Int.*, 168, 315–331.
- Lamb, H. (1910), On atmospheric oscillations, *Proc. R. Soc. London Ser. A*, 84, 551–572.
- Lamb, H. (1945), *Hydrodynamics*, Dover, New York.
- Ledoux, P., and T. Walraven (1958), Variable stars, *Handb. Phys.*, 51, 353–604.
- Lognonné, P. (2010), Seismic waves from atmospheric sources and atmospheric/ionospheric signatures of seismic waves, in *Infrasound Monitoring for Atmospheric Studies*, edited by A. Le Pichon et al., pp. 281–304, Springer Sci., New York.
- Lognonné, P., E. Clévédy, and H. Kanamori (1998), Computation of seismograms and atmospheric oscillations by normal-mode summation for a spherical earth model with realistic atmosphere, *Geophys. J. Int.*, 135, 388–406.
- Love, A. E. H. (1911), *Some Problems of Geodynamics*, Cambridge Univ. Press, Cambridge, U. K.
- Mikumo, T. (1968), Atmospheric pressure waves and tectonic deformation associated with the Alaskan earthquake of March 28, 1964, *J. Geophys. Res.*, 73, 2009–2025.
- Mikumo, T., and B. A. Bolt (1985), Excitation mechanism of atmospheric pressure waves from the 1980 Mount St. Helens eruption, *Geophys. J. Astron. Soc.*, 81, 445–461.
- Mikumo, T., and S. Watada (2010), Acoustic-gravity waves from earthquake sources, in *Infrasound Monitoring for Atmospheric Studies*, edited by A. Le Pichon et al., pp. 263–279, Springer Sci., New York.
- Mikumo, T., T. Shibusaki, A. L. Pichon, M. Garces, D. Fee, T. Tsuyuki, S. Watada, and W. Morii (2008), Low-frequency acoustic-gravity waves from coseismic vertical deformation associated with the 2004 Sumatra-Andaman earthquake, *J. Geophys. Res.*, 113, B12402, doi:10.1029/2008JB005710.
- Nishida, K., N. Kobayashi, and Y. Fukao (2000), Resonant oscillations between the solid earth and the atmosphere, *Science*, 287, 2244–2246.
- Pekeris, C. L. (1939), The propagation of a pulse in the atmosphere, *Proc. R. Soc. London Ser. A*, 171, 434–449.
- Pekeris, C. L. (1948), The propagation of a pulse in the atmosphere. Part II, *Phys. Rev.*, 73, 145–154.
- Pekeris, C. L., and H. Jarosch (1958), The free oscillations of the Earth, *Contribution in Geophysics in Honor of Beno Gutenberg*, vol. 1, edited by H. Benioff et al., pp. 171–192, Pergamon, New York.
- Phinney, R. A., and R. Burridge (1973), Representation of the elastic-gravitational excitation of a spherical earth model by generalized spherical harmonics, *Geophys. J. Astron. Soc.*, 34, 451–487.
- Pierce, D. A. (1966), Justification of the use of multiple isothermal layers as an approximation of the real atmosphere for acoustic-gravity wave propagation, *Radio Sci.*, 1, 265–267.
- Pierce, D. A. (1968), Theoretical source models for the generation of acoustic-gravity waves by nuclear explosions, in *Acoustic-Gravity Waves in the Atmosphere*, edited by T. M. Georges, pp. 9–24, U.S. Gov. Print. Off., Washington, D. C.
- Pierce, D. A., and J. W. Posey (1970), Theoretical prediction of acoustic-gravity pressure waveforms generated by large explosions in the atmosphere, final report, Air Force Cambridge Res. Lab., Bedford, Mass.
- Press, F., and D. G. Harkrider (1962), Properties of acoustic gravity waves in the atmosphere, *J. Geophys. Res.*, 67, 3889–3908.
- Press, F., and D. G. Harkrider (1966), Air-sea waves from the explosion of Krakatoa, *Science*, 154, 1325–1327.
- Press, W. H., S. T. Teukolsky, W. T. Vetterling, and B. P. Flannery (1992), *Numerical Recipes*, 2nd ed., Cambridge Univ. Press, Cambridge, U. K.
- Saito, M. (1988), DISPER80: A subroutine package for the calculation of seismic normal-mode solutions, in *Seismic Algorithms*, edited by D. J. Doornbos, pp. 293–391, Academic, New York.
- Takeuchi, H., and M. Saito (1972), Seismic surface waves, in *Methods in Computational Physics*, vol. 11, edited by B. A. Bolt, pp. 217–295, Academic, New York.
- Tanimoto, T. (1999), Excitation of normal modes by atmospheric turbulence: Source of long-period seismic noise, *Geophys. J. Int.*, 136, 305–402.
- Unno, W., Y. Osaki, H. Ando, H. Saio, and H. Shibahashi (1989), *Nonradial Oscillations of Stars*, 2nd ed., Tokyo Univ. Press, Tokyo.
- U.S. Standard Atmosphere (1976), *Committee on the Extension to the Standard Atmosphere*, U.S. Government Printing Office, Washington.
- Watada, S. (2009), Radiation of acoustic and gravity waves and propagation of boundary waves in the stratified fluid from a time-varying bottom boundary, *J. Fluid Mech.*, 627, 361–377, doi:10.1017/S0022112009005953.
- Widmer, R., and W. Zürn (1992), Bichromatic excitation of long-period Rayleigh and air waves by the Mount Pinatubo and El Chichón volcanic eruptions, *Geophys. Res. Lett.*, 19, 765–768.
- Woodhouse, J. H. (1988), The calculation of eigenfrequencies and eigenfunctions of the free oscillations of the Earth and the Sun, in *Seismic Algorithms*, edited by D. J. Doornbos, pp. 321–370, Academic, New York.
- Woodhouse, J. H., and T. P. Gornius (1982), Surface waves and free oscillations in a regionalized earth model, *Geophys. J. Astron. Soc.*, 68, 653–673.
- Yamamura, K., and H. Kawakatsu (1998), Normal mode solutions for radiation boundary conditions with an impedance contrast, *Geophys. J. Int.*, 134, 849–855.
- Yuan, X., R. Kind, and H. A. Pedersen (2005), Seismic monitoring of the Indian ocean tsunami, *Geophys. Res. Lett.*, 32, L15308, doi:10.1029/2005GL023464.

H. Kanamori, Seismological Laboratory, California Institute of Technology, 1200 E. California Blvd., MS 252-21, Pasadena, CA 91125-2100, USA. (hiroo@gps.caltech.edu)

S. Watada, Earthquake Research Institute, University of Tokyo, 1-1-1 Yayoi Bunkyo-ku, Tokyo 113-0032, Japan. (watada@eri.u-tokyo.ac.jp)